מכון ויצמן למדע
WEIZMANN INSTITUTE OF SCIENCE

A mechanism for the abrupt warming and simultaneous ice sheet discharge involved in Heinrich Events

By: Yohai Kaspi

Advisor: Prof. Eli Tziperman

Thesis for the degree of M.Sc.
Submitted to the Scientific Council
of the Weizmann Institute of Science
Rehovot, Israel

תיזה ל"מוסמך"
מוגש למועצה המדעית
של מכון ויצמן למדע
רחובות, ישראל

July 2002

Abstract

Abrupt climate changes known as Heinrich events have dominated the last glacial period. These events have been attributed to the internal instabilities of the Laurentide ice sheet, though seem to have affected climate throughout the northern hemisphere. In this study we use a coupled atmosphere-ocean-sea ice and land ice model to propose a novel mechanism for the dynamics of Heinrich events. This mechanism relies on the strong influence of a fresh water flux into the ocean during glacier collapse and the crucial role of sea ice due to the strong sea ice albedo feedback. This proposed mechanism suggests an explanation to two yet unexplained phenomena: The abrupt atmospheric heating after each Heinrich event, and the simultaneous discharge of ice from different ice sheets. A thorough description of this model is provided and then an explanation of the proposed mechanism.

Acknowledgments

I would like to thank Prof. Eli Tziperman who through many hours of devoted and patient supervision has introduced me to the subject and the concept of joint research. Eli's door was always open for my continuous questions, generously sharing with me his deep knowledge. I would like to also thank my officemates Eli Galanti, Roiy Sayag and Laure Zanna for their help with me computer ignorance.

Contents

1 Introduction

1.1 Heinrich events

Over the past glacial period (20 kyr BP - 100 kyr BP) earth's climate has been extremely variable on time scales of 1-10 kyr, and has experienced large scale oscillations, between glacial and interstadial conditions.

Heinrich (1988) observed 6 distinct layers of ice rafted debris (IRD) in a deep core of the Northern Atlantic (blue dot, Fig. 2). These layers, spaced in intervals of 7,000-10,000 years, occurred between the beginning and the termination of the last glaciation. More precisely later evidence point the last Heinrich event (H1) to 15 kyr BP, H2 to 22 kyr BP, H3 to 27 kyr BP, H4 to 35 kyr BP and H5 to 44 kyr BP.

Four years later more evidence for the existence of these layers were found (Broecker et al., 1992; Bond et al., 1992), with the discovery of similar IRD's in other regions of the Northern Atlantic. The high concentration of detrital carbonate that originates in the limestone that underlies Hudson Bay Broecker and Hemming (2001) and Hudson strait (yellow area, Fig. 2), and the geochemical signature of the noncarbonate fraction, had suggested that the origin of these layers is from these areas of Northern Canada. The detrital carbonate could be traced for more than 3000 km, a remarkable distance, in a series of cores across the Atlantic. These cores are placed in a broad arc (yellow dots, Fig. 2), while north and south of this arc no detrital carbonate is present. Furthermore, while the detrital carbonate layers in the Labrador sea are several meters thick, the detrital carbonate found in the Eastern North Atlantic are only several cm thick. All these evidences pinpointed the origin of these layers to parts of the Laurentide ice sheet (LIS) over Hudson Bay, and brought most to believe that some abrupt events had caused collapses in the LIS and the release of iceberg armadas into the northern Atlantic.

Evidence from the Greenland ice core project (GRIP - black dot, Fig. 2) have linked the Heinrich events to rapid oscillations in air temperature over Greenland Dansgaard et al. (1993). According to these records (Fig. 1), Heinrich events occurred at the end of cold periods of several thousand years, and were followed by abrupt warmings to almost interglacial temperatures, which began less than a thousand years after the IRD discharge, and lasted for between several hundred and several thousand years.

Bond et al. (1993) also linked Heinrich events to changes in the sea surface temperature (SST). They showed that most Heinrich events occurred during times of cold SST and lowered surface salinities, probably caused largely by melting of drifting ice. After each event, there was a jump of up to 10 C in the SST (at latitude 50N) followed by progressive cooling, over a few hundred years.

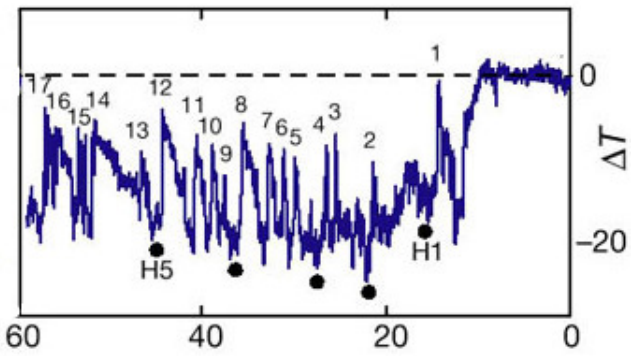

Figure 1: Record of $\delta^{18}O$ from the GRIP core, a proxy for atmospheric temperature over Greenland. The D/O events are numbered and the Heinrich events 1-5 are marked by dots. (Taken from Ganopolski and Rahmstorf (2001))

1.2 Dansgaard Oeschger events and the Bond cycle

The oxygen isotope measurements in Greenland ice cores show also a series of higher frequency warm-cold oscillations called Dansgaard Oeschger events Dansgaard et al. (1984) which punctuated the last glaciation. The D/O events typically start with an abrupt warming of 5-10 C over a few decades or less, followed by a gradual cooling that lasts 1500 years, or with a decreasing probability, 3000 or 4500 years Alley et al. (2001). D/O events are well synchronized with the Heinrich events, occurring usually three times between each Heinrich event. Progressive cooling through several such D/O cycles, which ends with a Heinrich event followed by an abrupt warming to almost interglacial temperatures, defines what is known as a Bond cycle Alley (1998). These evidences are seen best in the $\delta^{18}O$ record from the GRIP ice core from Greenland's summit in Fig 1. Although having a less clear imprint, the D/O and Bond cycle can be traced also in SST anomalies Bond et al. (1993).

1.3 Synchronized events

After an assumption for the origin of the Heinrich events IRD's has been established, evidence of IRDs from different sources began to emerge. In 1995 Bond and Lotti (1995) compared the abundances of many types of lithic grains from several sites in the eastern North Atlantic (red dots, Fig. 2), and found distinct peaks of three different types; basaltic glass derived from Iceland, grains with hematite coating derived from several regions of the Northern Atlantic (mostly around the gulf of St. Lawrence), and the detrital carbonate from Hudson bay. In addition to peaks of detrital carbonate during H1, H2, H3, H4 (H3 has a weaker signal), they also found basaltic glass derived from Iceland just prior to each event. More surprisingly they found lithic peaks of this origin during most of the D/O events, and some of them with peaks reaching as high as during the

Heinrich events. This suggests that during the surge of the LIS there was a synchronous surge of the Icelandic ice sheet. The Icelandic source of the basaltic glass is confirmed in the presence of correlatives of the peaks in a core much closer to Iceland (orange dot, Fig. 2), and by evidence that peak abundances of basaltic glass in that core are much larger than in the eastern North Atlantic. The grains with hematite coatings are harder to trace, but a comparison of their abundance from different sites led to the conclusion that their origin is from ice caps within or near the Gulf of St. Lawrence. As the grains from of the Icelandic origin, they too correlate well with the D/O and Heinrich events.

The Irminger basin is the major passage for icebergs from the Greenland, Norwegian and Arctic seas into the Atlantic, and therefore analysis of cores from this area is essential for analyzing other glacial surges. Oxygen isotope of foraminifera and IRD records from the Irminger basin Elliot et al. (1998) (dark green dot, Fig. 2), give further clues regarding the origin and global synchronization of the Heinrich events. Five of the IRD peaks from the Irminger basin have ages analogous to the Heinrich events 1-5. Here, unlike in midlatitude sediment cores, detrital carbonate (indicator to LIS source) was not found and the most traceable origin was again only the Icelandic ice sheet. As in Bond and Lotti (1995) numerous IRD peaks in between Heinrich events appear, though only the Heinrich events can be associated with $\delta^{18}O$ anomalies in marine sediments, indicating increased SST or low sea surface salinity. The SST anomalies contribute to the assumption that Heinrich events were a large scale phenomena affecting also the SST while the more rapid millennium timescale instabilities are associated with more local surges from ice sheets from the Nordic regions. Nevertheless, the fact that most Heinrich events are preceded by one of the smaller IRD discharges, may indicate that the "smaller-scale" iceberg surges are somehow linked to the massive collapses of the LIS. In addition, foraminiferal abundance from the Irminger basin, which is low during most of the glacial period, increases within each IRD layer, and could be indicative of oscillations of the sea ice limit Elliot et al. (1998). Unlike midlatitude cores which show a large increase in SST after most Heinrich events, the Irminger basin core's imprint is much more modest. The range for summer SST variation is only a few degrees, usually lagging after the midlatitude cores, implying northward propagation of meltwater from the midlatitudes after the events. This northward shift of the polar front at the end of each Heinrich event, may reflect the rapid switch to a more active thermohaline circulation.

It seems that other ice sheets may also be linked to the LIS surges. Sediment, microfossil and oxygen isotope data Fronval et al. (1995) from a sediment core in the Norwegian sea, close to the Scandinavian shore line (purple dot, Fig. 2), reveal cooling events and iceberg discharge analogous to the Heinrich events. These results, although less conclusive than the results of the Icelandic ice sheet, seem to show that the fluctuations in the Norwegian sea are phase locked with changes in air temperature over Greenland: when air temperature over Greenland decreases, the deposition

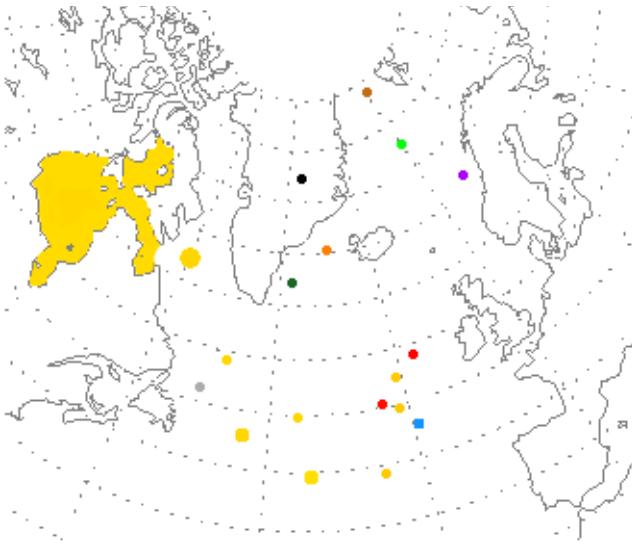

Figure 2: Location of cores containing IRD's mentioned in the text. The Yellow area marks areas rich in detrital carbonate, yellow dots mark cores with detrital carbonate, where the bigger the dot the thicker is the IRD layer.

of glacial debris in the Norwegian sea increases. The limestone poor IRD composition, points to local sources from Southern Scandinavia or the Baltic region. This IRD correlation implies that the Fennoscandian and Laurentide ice sheets fluctuated coherently with oceanic and atmospheric heat transports. On the contrary, other evidence Dowdeswell et al. (1999) from the Nordic seas (further off the cost of Scandinavia) show lack of correlation to all Heinrich events, although even they identify ten well defined IRD peaks in the interval between H6 and H1. Out of the ten IRD peaks in their analysis two do correlate with Heinrich layers (H2 and H3) . This varied evidence suggests that correlation between the Fennoscandian and Laurentide ice sheets may have been more complicated than initially suggested, but some correlation between rapid ice sheet surges of areas of the Fennoscandian ice sheet and the Laurentide ice sheet does exist.

There is additional evidence of ice sheet surges from other ice sheets during specific Heinrich events. During the last glacial maxima a marine based ice sheet covered the Barents sea. A dramatic shift in sediment core composition Bischof (1994) from the Norwegian sea (light green dot, Fig. 2) suggests that rapid and almost complete deglaciation of this ice mass took place almost simultaneously (14.5 kyr) with H1. Also an oxygen isotope anomaly in the Fram Strait (Norwegian sea) (brown dot, Fig. 2) from around the same time, has been attributed to an initial meltwater pulse from the deteriorating Barents ice sheet Jones and Keigwin (1988). Other data suggesting synchronization between different ice sheets were presented by McCabe and Clark (1998) who show a rapid retreat in the position of the British ice sheet after H1.

1.4 Existing theories of Heinrich and Dansgaard-Oeschger events

Soon after the origin of the Heinrich event was tracked down to the LIS collapse and to Hudson bay, MacAyeal suggested a simple model MacAyeal (1993a) ,MacAyeal (1993b) for the periodic oscillations in the IRD record. He called it the binge-purge oscillator; As the LIS thickened in the region of Hudson bay, geothermal heat gradually warmed the ice sheet base until basal melting occurred. The base melt reduced the friction of the ice sheet with its bottom boundary, and caused vast amounts of glacier mixed with the soft material underlying Hudson bay to be flushed out into the Labrador sea, and from there carried by winds and currents eastward to the Atlantic ocean. Meanwhile the initial glacier has become thiner, allowing the geothermal heat to diffuse out.This led to a refreezing of the base, and the ice sheet once again began to thicken, initiating another cycle. This hypothesis is consistent with the 10^4 year spacing of these events, but the time scale depends on specified parameters such as the atmospheric temperature above the ice, and the accumulation rate of snow over the ice sheet. Also, the binge-purge mechanism did not account for the abrupt warmings after the events and for the simultaneous ice sheet collapse events on both sides of the Atlantic.

Later, after the Heinrich Events were recognized as a more global phenomena, other models mostly dealing with the effect of a sudden input of fresh water into the thermohaline circulation (THC) emerged. Ganopolski and Rahmstorf (2001) used an intermediate complexity ocean-atmosphere model, to examine the influence of a freshwater perturbation into the northern seas on the THC, while varying this fresh water perturbation both in strength and in meridional location. They suggested that the ocean circulation operates in two distinctly different regimes, an interglacial and a glacial regime. Transitions between on and off modes during the glacial regime can be triggered by small changes in freshwater flux Stocker et al. (1992); Broecker et al. (1990). The glacial regime exists because during glacials (cold periods) the North Atlantic Deep Water (NADW) is formed southward than presently. Both D/O and Heinrich events are demonstrated by imposing a freshwater perturbation (0.03 Sv and 0.15 Sv respectively). The D/O events trigger massive convection in the northern seas leading to increased NADW of up to 45 Sv and settle back to normal conditions after a time scale of about 1000 years, this causes also increase in the atmospheric temperature over Greenland as observed in the paleorecords. Imposing a stronger fresh water flux representing the Heinrich events causes a shut off of the conveyor belt and no variation in Greenland temperatures. Although this model creates millennial scale oscillations in response to fresh water forcing, it seems that the NADW response may be too dramatic (40 Sv increase over decades). Also the fresh water fluxes are externally imposed in the model and their periodicity is not explained in the proposed mechanism.

Timmermann et al. (2002) show that millennial time scale oscillations can be excited stochas-

tically, once the North Atlantic ocean is fresh enough. They hypothesize that D/O events are the joint result of stochastic freshwater forcing and Heinrich events. Their results show millennial scale oscillations as a response to fresh water forcing, but with strong dependence on both the amplitude of the forcing and the stochastic freshwater noise. They use fresh water fluxes of different strengths and different time scales to represent the Heinrich events, and as in Ganopolski and Rahmstorf (2001) they also externally impose these fluxes into the model.

1.5 This study

The objective of the present study is to address two main issues. One is to try and understand the mechanism that caused warmings to almost interglacial temperatures following the Heinrich events. The second is to explain the synchronous ice surges from different ice sheets.

In order to try and answer these questions, we built a simple land ice-ocean-sea ice-atmosphere model. We use MacAyeal's Binge-Purge oscillator MacAyeal (1993a,b) model in order to produce ice sheet relaxation oscillations. The idea is that these oscillations then trigger changes in the otherwise stable thermohaline circulation, and create a disturbance which effects the coupled ocean-atmosphere system. The ocean affects the atmosphere mainly through the albedo effect of the sea ice, and the atmospheric model, in turn, determines the accumulation and ablation rates in the land ice model, thus closing the coupling loop. The model is described in detail in section 2.

Section 3 presents the results of the ocean-atmosphere model coupled to a single binge-purge ice sheet oscillator. In this section our new slush-flush binge-purge mechanism demonstrated by this model is presented, which explains the abrupt atmospheric warmings after the IRD discharges.

In section 4 more ice sheets are added to the model in order to simulate the coupling between the Laurentide ice sheet and the European ice sheets.

Section 5 is devoted to a parameter sensitivity study, where we go over each of the parameters introduced in the model, and check its effect on our proposed mechanism.

2 Model Description

2.1 Land ice Model

The land ice model follows MacAyeal's model [1993 a,b]. In this model, land ice thickness $H(t)$ is assumed to be uniform along the two dimensional cross section representing the part of the Laurentide ice sheet over Hudson bay. The bed on which the land ice lies is assumed to be flat and at sea level. The ice sheet is geothermally heated from below, and once the ice sheet base is melted, the ice is free to flow off the rigid bed into the ocean. The model therefore has two stages:

the accumulation (binge) stage while the bed is frozen and the collapse (purge) stage while the base is melted.

2.1.1 Binge stage

The height of the land ice glacier is determined by the snow accumulation rate, (given by the atmospheric model), minus the ablation rate,

$$\frac{dH(t)}{dt} = Acc(t) - Abl(t) \tag{1}$$

The glacier heat equation, is a diffusion equation (neglecting advection terms)

$$\frac{\partial T(t,z)}{\partial t} = \frac{\kappa}{C_p^{ice}\rho^{ice}} \frac{\partial^2 T(t,z)}{\partial z^2} \tag{2}$$

Changing the variable z to the independent variable ζ, defining $\zeta = \frac{z}{H(t)}$ we find (see Appendix A1)

$$\frac{\partial T(t,\zeta)}{\partial t} = \frac{\kappa}{C_p^{ice}\rho^{ice}H(t)^2} \frac{\partial^2 T(t,\zeta)}{\partial \zeta^2} + \frac{\partial T(t,\zeta)}{\partial \zeta(t)} \frac{\zeta(Acc(t) - Abl(t))}{H(t)} \tag{3}$$

The lower boundary condition ($\zeta = 0$) of the heat equation is a specified heat flux equal to the geothermal heat flux (G), from earth's interior below the ice, and is assumed here constant in time. The upper boundary condition ($\zeta = 1$) is that the upper temperature is given by the atmospheric temperature above the ice sheet. The atmospheric temperature above the ice sheet comes from the atmospheric model, taking into consideration a lapse rate of, $\Gamma = 9\frac{^oC}{km}$ as in MacAyeal (1993a). Therefore the two boundary conditions of the heat equation during the binge stage are

$$\frac{\partial T(t,0)}{\partial \zeta(t)} = \frac{H(t)G}{\kappa} \tag{4}$$

$$T(t,1) = \theta(t) - \Gamma H(t) \equiv T_{top}(t), \tag{5}$$

where $\theta(t)$ is the temperature of the atmosphere, and κ is the ice thermal conductivity.

The accumulation rate at a time t is determined by the height of the glacier at that time, and the fresh water flux from the atmospheric model ($Q_S^{atm-ocean}$). The accumulation rate decays exponentially with increasing ice sheet surface elevation to reflect the reduction of precipitable water vapor at higher elevation

$$Acc(t) = \frac{Q_S^{atm-ocean}}{Area} * e^{\frac{-H(t)}{Z_0}}, \tag{6}$$

where the accumulation rate scale hight Z_0 is chosen to reflect a reasonable accumulation decay (see section 5.8), and $Area$ is the area of the ice sheet.

The Ablation is considered negligible for $T(\zeta = 1) = T_{top} < 0^oC$ (since the glaciers are at high latitudes this is almost always the case at the top of the glacier), the ablation for $T_{top} > 0^oC$ will be $Abl = \beta * T_{top}$, where $\beta = 6.3 \frac{mm}{day*K}$ Braithwate (1981).

2.1.2 Purge stage

Since the heating of the land ice sheet is primarily from below, a negative vertical temperature gradient exists in the glacial column. Once the basal temperature reaches the melting temperature, the system switches into the purge stage. Now vast amounts of fresh water glaciers are released into the ocean. The thinning rate of the ice column will be a function of its thickness as seems to be the case for ice streams in Antarctica MacAyeal (1989). A simple equation which captures this relationship is,

$$\frac{dH(t)}{dt} = -\frac{H(t)}{\tau} \tag{7}$$

so that the height of the glacier decays exponentially with the time scale τ, taken to be 250 years to reflect the short timescale of the purge, as seen in the evidence from the IRD records.

The heat equation remains the same as in the binge stage, except that the term coming from the height equation changes (Appendix A1), therefore

$$\frac{\partial T(t,\zeta)}{\partial t} = \frac{\kappa}{Cp_{ice}\rho_{ice}H(t)^2}\frac{\partial^2 T(t,\zeta)}{\partial \zeta^2} - \frac{\partial T(t,\zeta)}{\partial \zeta(t)}\frac{\zeta}{\tau} \tag{8}$$

At the lower boundary ($\zeta = 0$) the temperature is just set to the melting temperature, and the upper boundary condition, at ($\zeta = 1$) is set just as in the binge stage

$$T(t,0) = 0 \tag{9}$$

$$T(t,1) = \theta(t) - \Gamma H(t) \tag{10}$$

During the purge stage, the temperature at the base is influenced by frictional heat at the base, due to the horizontal sliding of the ice. The base remains melted until the diffusive heat flux driven by the vertical temperature gradient exceeds the combined heat flux of the geothermal heat and the frictional heat. Under the assumption that the rate of frictional heating at the base is proportional to the rate at which the gravitational potential energy stored in the ice column is lost by thinning, the basal heating rate per unit area due to friction is given by

$$-\frac{d}{dt}\left(\frac{1}{2}\rho_{ice}gH(t)^2\right) = -\rho_{ice}gH(t)\frac{dH(t)}{dt} = \frac{\rho_{ice}gH(t)^2}{\tau}$$

Parameter	Meaning	Value	Units
Γ	Lapse rate	0.009	$m^o C^{-1}$
τ	Decay time	7.88E9	s
κ	Ice thermal conductivity	2	$Watt\, m^{-1}\, ^o C^{-1}$
G	Geothermal heat flux	0.05	$Watt\, m^{-2}$
g	Gravitational Acceleration	9.8	$m\, s^{-2}$
β	Ablation rate	7.29E-8	$m\, s^{-1}\, ^o C^{-1}$
Cp_{ice}	Specific heat of ice	2061	$Watt\, Kg^{-1}\, ^o C^{-1}$
ρ_{ice}	Mean density of ice	917	$Kg\, m^{-3}$
ρ_{water}	Mean density of water	1028	$Kg\, m^{-3}$
Z_0	Accumulation rate scale height	1000	m
$Area$	Area of land glacier	1E12	m^2

Table 1: Parameters for the land ice model

Thus the condition for switching from purge stage to binge stage is

$$\frac{dT(t,\zeta)}{d\zeta} > -\left(\frac{H(t)G}{\kappa} + \frac{\rho_{ice} g H(t)^3}{\tau\kappa}\right). \tag{11}$$

The volume of fresh water per unit time that the land ice glacier releases into the ocean during the collapse stage is given by the following expression

$$Q_S^{landice-ocean} = Area \frac{dH(t)}{dt} \frac{\rho_{ice}}{\rho_{water}}. \tag{12}$$

2.2 Ocean Model

The ocean model is a standard (northern) hemispheric meridional 4-box model Stommel (1961); Gildor and Tziperman (2001). The two upper boxes represent the above thermocline water and have a depth of 400m, while the lower boxes represent the deep ocean, with a depth of 3600m. Latitude 60N is the division line between the southern and northern boxes (see Fig. 3 & 4).

The model dynamics include a simple linear frictional horizontal momentum balance and are hydrostatic and mass conserving (See Appendix A2 for the derivation). Thus the governing equations for the dynamics in the y (northward) and z (upward) directions respectively are

$$\frac{\partial p}{\partial y} = -rv \tag{13}$$

$$\frac{\partial p}{\partial z} = -\rho g \tag{14}$$

where p denotes pressure, v is the northward velocity, r is a friction coefficient, ρ the water density

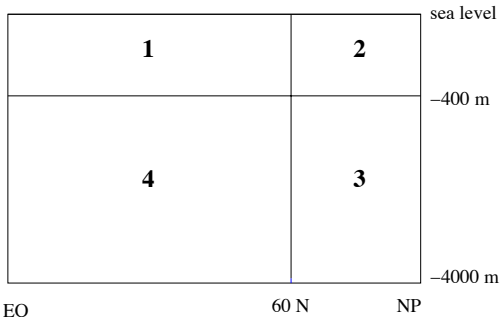

Fig 3: The 4 box ocean model.

and g is the gravitational acceleration.

Using these two equations and assuming conservation of mass, we can find (Appendix A3) that the transport (U) between the boxes in this 4 box model is given by

$$U = C_u g\left[(\rho_2 - \rho_1)D_{upper} + (\rho_3 - \rho_4)D_{lower}\right] \tag{15}$$

The evolution of the Temperature (T) and Salinity (S) is given by the following advection-diffusion equations

$$\frac{\partial T}{\partial t} + \nabla(T\mathbf{u}) + \kappa\nabla^2 T = 0 \tag{16}$$

$$\frac{\partial S}{\partial t} + \nabla(S\mathbf{u}) + \kappa\nabla^2 S = 0 \tag{17}$$

where $\mathbf{u}$ is the vector velocity and κ is the diffusion coefficient. Integrating over the volume of a box i, assuming incompressibility, and assuming the boundary fluxes are zero we find the heat equation for box i

$$\begin{aligned}\frac{\partial T_i}{\partial t} = \frac{1}{D_i W_i L_i}\Bigg[&U(T_j - T_i) + \frac{\kappa_h D_i W_i (T_k - T_i)}{0.5(L_k + L_i)} + \frac{\kappa_v D_i W_i (T_m - T_i)}{0.5(D_m + D_i)} \\ &+ W_i L_i (Q_T)_i^{atm-ocean} + W_i L_i (Q_T)_i^{seaice-ocean}\Bigg]\end{aligned} \tag{18}$$

where D_i, W_i, L_i are the depth, width and length of box i respectively, and κ_v, κ_h are the vertical and horizontal diffusion coefficients respectively. The indices j,k,m are the indices of the neighboring boxes to box i in the following manner

$$\begin{aligned} j &= \begin{cases} i-1 \mod(4) & if \quad U > 0 \\ i+1 \mod(4) & if \quad U < 0 \end{cases} \\ k &= (2,1,4,3) \quad for \quad i = (1,2,3,4) \\ m &= (4,3,2,1) \quad for \quad i = (1,2,3,4) \end{aligned}$$

The interaction with atmosphere and sea ice terms (last two terms) apply, of course only for the surface boxes (boxes 1,2)

The atmosphere-ocean heat flux term depends on the temperature difference between the atmosphere and ocean, and on the depth of the ocean box. We introduce a typical timescale for this interaction $\tau^{atm-ocean}$. This time scale determines the rate of the heat transfer (see discussion in section 5.6) between the ocean and atmosphere, which is chosen such that the heat transport to the northern polar atmospheric box is about 1 PW on average. In addition we add a factor that represents the insulating effect of the sea ice Walsh (1982); Bryan et al. (1974).

$$(Q_T)_i^{atm-ocean} = \frac{(\theta_i - T_i)D_{upper}}{\tau^{atm-ocean}} \left[(1 - frac^{seaice}) + frac^{seaice} (\frac{0.05}{1.7 + thickness}) \right] \tag{19}$$

where θ_i is the temperature in the corresponding atmospheric box, and the $frac^{seaice}$ and $thickness$ variables are calculated in the sea ice section.

The sea ice-ocean flux is the flux transferred between the ocean and the sea ice during the creation or melting of sea ice and is given by

$$(Q_T)_i^{seaice-ocean} = \frac{(T^{seaice} - T_i)D_{upper}}{\tau^{seaice-ocean}}. \tag{20}$$

where T^{seaice} is the freezing temperature of the surface box, and $\tau^{seaice-ocean}$ is the typical time scale for creation of sea ice (see sensitivity to these parameters in section 5.4). This term is the change in heat necessary for the creation or melting of sea ice.

The salinity equations can be derived similarly, the only difference is that the salinity equations include the fresh water flux from the land ice model into box 2 (the corresponding heat term is negligible), so the equations for the salinity in the upper boxes are

$$\begin{aligned} \frac{\partial S_i}{\partial t} &= \frac{1}{D_i W_i L_i} \left[U(S_j - US_i) + \frac{\kappa_h D_i W_i (S_k - S_i)}{0.5(L_k + L_i)} + \frac{\kappa_v D_i W_i (S_m - S_i)}{0.5(D_m + D_i)} \right. \\ &+ \left. W_i L_i (Q_S)_i^{atm-ocean} + W_i L_i (Q_S)_i^{seaice-ocean} + W_i L_i (Q_S)_i^{landice-ocean} \right] \end{aligned} \tag{21}$$

where the indices are as denoted in (18), $Q_S^{landice-ocean}$ comes from the land ice model (12), $Q_S^{seaice-ocean}$ from the sea ice (24), and $Q_S^{atm-ocean}$ from the meridional fresh water flux in the atmospheric model (34).

Equation of state

The two thermodynamic variables are the temperature and salinity, and the equation of state $\rho = \rho(T,S)$ is the full nonlinear equation recommended by UNESCO (1981), Gill (1982, Appendix 3).

Parameter	meaning	Value	Units
D_{upper}	Depth of the upper ocean box	400	m
D_{lower}	Depth of the lower ocean box	3600	m
L_{north}	Length of the northern boxes	3.329E6	m
L_{south}	Length of the southern boxes	6.658E6	m
W	Width of all boxes	6.3E6	m
g	Gravitational acceleration	9.8	ms^{-2}
C_u	Transport coefficient	14300	$m^4 sKg^{-1}$
C_p^{water}	Specific heat of water	4185	$JKg^{-1}{}^oK^{-1}$
T^{seaice}	Mean box temp for creation of seaice	1	${}^oC$
ρ_{ice}	Mean density of ice	917	Kgm^{-3}
ρ_{water}	Mean density of water	1028	Kgm^{-3}
L_f	Latent heat water-ice phs. trans.	3.34E5	JKg^{-1}
κ_v	Vertical diffusion constant	8E-5	ms^{-2}
κ_h	Horizontal diffusion constant	8E3	ms^{-2}
$\Delta\rho_{con}$	Convection density scale	0.02	Kgm^{-3}
$\tau^{atm-ocean}$	Typical timescale Atm-Ocn	4	*years*
$\tau^{seaice-ocean}$	Seaice restoring time	1	*years*
τ_{con}	Convection typical timescales	30,270	*days*

Table 2: Parameters for the ocean model

Convection

Once the density of the upper box exceeds that of the lower box, convective mixing between two vertical boxes occurs. In order to smoothly parameterize this mixing we use a hyperbolic tangent profile. Therefore we add to the temperature (same for salinity) equation, a term similar to:

$$\frac{D_i W_i L_i (T_i - T_j)}{\tau_{con}} \tanh\left[\frac{\rho_i - \rho_j}{\Delta\rho_{con}}\right]$$

Where i ,j are the two boxes being mixed, τ_{con} is the convection timescale, and $\Delta\rho_{con}$ is a density scale.

Thermohaline Circulation

The THC in this model is represented through the linear transport equation (15). This parameterization for the THC is rather simple and may not be enough. Due to the total dependence on density gradients and the positive advection feedback mechanism (see section 3.2) it turns out that this parameterization allows the THC to be shut down, while recent evidence Legrand and Wunsch (1995) suggest that the THC had never been shut down. Therefore we set a boundary limit for the THC at 6 Sv. In section 5.1 we show that our mechanism is totally independent of this limit, and we can obtain the same cycle for an unbounded THC, and for a higher bounded THC. This limit is

set only in order to get a more "real" THC.

2.2.1 Sea ice

Sea ice forms when the ocean box temperature (box 2) drops below the freezing point. Since the model temperature represents the mean temperature in the box, we take T^{seaice} to be more than the actual freezing temperature of ocean water. The heat flux $Q_T^{seaice-ocean}$ is converted into the amount of sea ice created (or melted) by

$$\frac{dV_i^{seaice}}{dt} = \left(\frac{(Q_T)_i^{seaice-ocean} \cdot C_p^{water} \rho^{water} - SW_i^{seaice}}{\rho^{ice} L_f} + P_i^{on-ice} \right) W_i L_i \tag{22}$$

where P_i^{on-ice} is the amount of sea ice created by the precipitation accumulated directly on the sea ice, which is given by

$$P_i^{on-ice} = (Q_S)_i^{atm-ocean} frac_i^{seaice} \frac{\rho^{water}}{\rho^{ice}} \tag{23}$$

SW_i^{seaice} is the amount of sea ice melted directly by the penetration of the short wave radiation into the sea ice, as described below in the atmospheric model subsection.

Knowing the rate of change in the sea ice volume we can also determine the flux of fresh water from/to the sea ice

$$(Q_S)_i^{seaice-ocean} = \frac{dV_i^{seaice}}{dt} \frac{\rho^{ice}}{\rho^{water} W_i L_i}. \tag{24}$$

Assuming the sea ice grows with a constant thickness of 2 meters, $frac_i^{seaice}$ is given by

$$frac_i^{seaice} = \frac{V_i^{seaice}}{2 W_i L_i} \tag{25}$$

Only after the entire box is covered by sea ice (this can rarely happen see analysis in section 3.2) does sea ice thickness grow beyond 2 meters. In the sensitivity tests (section 5.4) we show that our proposed mechanism is not sensitive to any of the sea ice parameters; thickness, time scale and freezing temperature.

There are three contributors to the creation or melting of sea ice (22). Two of them, P^{on-ice} and SW^{seaice} exist only when some sea ice exists, thus the prime condition for the creation of sea ice, from an initial condition of no sea ice, is that the ocean temperature drops below the critical freezing temperature . Both terms P^{on-ice} and SW^{seaice} are invariant to this critical temperature, and only once sea ice is created, and the sea ice grows, do these two parameters grow as well. If this critical temperature was different, growth or melting may have been triggered at a different time, but the physical mechanism would have remained the same, because once sea ice is at equilibrium,

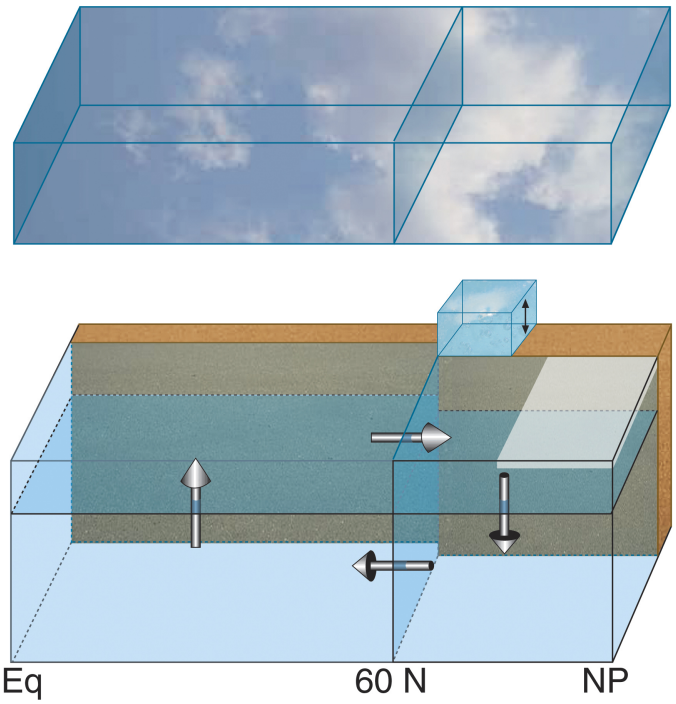

Fig 4. A schematic diagram of the coupled model. The arrows mark the direction of the THC.

the ocean box temperature T_i can change so that $T^{seaice} - T_i$ balances the contribution of the other two factors. The equilibrium balance of the sea ice is analyzed in more details in section 3.2.

The major dynamical role of the sea ice in this model is to affect earth's albedo due to the large difference between the ocean albedo and the sea ice albedo (in this model 0.55 and 0.1 respectively). The other important role of the sea ice is to act as an insulator between the ocean and the atmosphere (19). Thus once sea ice reaches equilibrium and if sea ice extent is large, the atmosphere and ocean temperatures may significantly diverge from each other.

2.3 Atmospheric Model

The Atmospheric model is a two box model similar to that of Rivin and Tziperman (1997) in which the horizontal box dimensions coincide with those of the upper ocean boxes.

The heating rate per unit mass, is given by Peixoto and Oort (1991)

$$Q = C_p^{air} T \frac{dln\theta}{dt}$$

where θ is the potential temperature at a pressure P relative to the reference pressure P_0, given by $\theta = T\left(\frac{P_0}{P}\right)^{\frac{R_d}{C_p^{air}}}$, C_p^{air} is the specific heat of air and R_d is the dry air constant. Taking the box model potential temperature to represent the potential temperature at half the surface atmospheric

pressure, we find that

$$\frac{\partial \theta}{\partial t} = \frac{Q}{C_p^{air}} 2^{\frac{R_d}{C_p^{air}}}$$

Expressing the heating rate as a divergence of the heat flux F, such that $Q = \frac{-\nabla F}{\rho_{air}}$, and integrating over the volume of the box we find

$$\frac{\partial \theta_i}{\partial t} = \frac{2^{\frac{R_d}{C_p^{air}}}}{C_p^{air} \rho^{air}} \left[F_i^{top} - F_i^{bottom} - \frac{D^{atm}}{L_i} F_i^{meridonal} \right]. \tag{26}$$

Using again the hydrostatic approximation $\frac{\partial p}{\partial z} = -\rho g$, and integrating, we find that $P_0 = \rho_{air} g D^{atm}$. Substituting in the former expression we find that

$$\frac{\partial \theta_i}{\partial t} = \frac{2^{\frac{R_d}{C_p^{air}}} g}{C_p^{air} P_0} \left[F_i^{top} - F_i^{surface} - \frac{D^{atm}}{L_i} F_i^{meridonal} \right], \tag{27}$$

where F_i^{top} is the net radiation at the top of the atmospheric box i, which is composed of the incoming shortwave radiation and the outgoing long-wave radiation. $F^{meridonal}$ is the heat flux between the two boxes, and $F_i^{surface}$ is the heat coming from the ocean.

The incoming radiation into the atmosphere is the short-wave radiation from the sun. Depending on earth's albedo (α_i^{tot}) some of this radiation is reflected back into space, and some is absorbed by earth and heats the atmosphere. Considering the relative distribution of land, ocean and sea ice in our model, earth's mean albedo at a given time can be estimated as

$$\alpha_i^{tot} = (1 - \alpha_i^{clouds}) \cdot \left\{ frac_i^{land} \alpha_i^{land} + (1 - frac_i^{land}) \cdot \left[frac_i^{seaice} \alpha^{seaice} + (1 - frac_i^{seaice}) \cdot \alpha^{ocean} \right] \right\} \tag{28}$$

The net incoming short-wave radiation (SW_i) is averaged over the area of each box. Although our model does not consider seasonal effects, the incoming radiation (especially in the polar box) varies considerably due to the changes in the declination of the earth's axis over the year. Therefore we also take into consideration the yearly variation of declination angels. The atmosphere emits long-wave radiation back to space, given by

$$LW_i = (P_i)_{lw} \sigma (\theta_i)^4, \tag{29}$$

where P_{lw} is the emissivity (see discussion in section 5.3), and σ is the Stephan-Boltzmann constant. Part of the net short-wave absorbed by the sea ice and denoted SW_i^{seaice}, does not contribute to the long-wave heating of the atmosphere, but contributes directly to melting of sea ice. We estimated this effect according to Maykut and Perovich (1987) (although the choice has a minor

Parameter	meaning	Value	Units
Cp_{air}	Specific heat of air	1004	$JKg^{-1}{}^{o}K^{-1}$
Cp_{water}	Specific heat of water	4185	$JKg^{-1}{}^{o}K^{-1}$
ρ_{water}	Mean density of water	1028	Kgm^{-3}
R_d	Dry air constant	287	$JKg^{-1}{}^{o}K^{-1}$
P_0	Pressure at surface level	1013	mb
κ_{mer}	Meridonal heat coefficient	1.35E20	$Jms^{-1}{}^{o}K^{-1}$
g	Gravitational acceleration	9.8	ms^{-2}
σ	Stephan Boltzman constant	5.68E-8	$Watt{}^{o}K^{-4}m^{-2}$
SW_i	Mean daily radiation from the sun	372,224	$Watt\,m^{-2}$
α_i^{land}	Average albedo of land	0.1,0.25	none
α^{clouds}	Average albedo of clouds	0.25	none
α^{seaice}	Average albedo on seaice	0.6	none
α^{ocean}	Average albedo on ocean	0.1	none
L_{north}	Length of the northern boxes	4.15E6	m
L_{south}	Length of the southern boxes	1E7	m
P^{seaice}	Penetrating parameter into seaice	0.25	none
P_{lw}	emissivity	0.55,0.61	none
L	Latent heat of evaporation	1.56E6	JKg^{-1}
C_{mer}	Saturation humidity constant	1.1E6	none
K_q	Meridional fresh water constant	7.95E14	m^3s^{-1}

Table 3: Parameters for the Atmosphere model

effect on the dynamics - see section 5.5), and it is given by

$$SW_i^{seaice} = SW_i P^{seaice}(1-\alpha^{clouds})(1-\alpha^{seaice})(1-frac^{land})frac_i^{seaice}, \tag{30}$$

where P^{seaice} is the percentage of the net short-wave received by the sea ice which goes to direct melting.

Given the above relations F_i^{top} is given by

$$F_i^{top} = SW_i(1-\alpha_i^{tot}) - SW_i^{seaice} - LW_i, \tag{31}$$

and $F_i^{surface}$ is the heat flux from the ocean given in the ocean model by $(Q_T)_i^{atm-ocean}$.

For the meridional heat transport we use

$$F^{meridional} = \frac{\kappa_{mer}}{D^{atm}W}\frac{\partial\theta}{\partial y},$$

where κ_{mer} is chosen such that the meridional atmospheric heat transport is about 1PW. In finite

difference form the meridional heat transport into atmospheric box i is

$$F_i^{meridional} = \frac{\kappa_{mer}}{D^{atm} W_i} \frac{\theta_j - \theta_i}{\frac{1}{2}(L_j + L_i)}. \tag{32}$$

where j denotes the other atmospheric box. The D^{atm} cancels in (27) and our equations are invariant to this factor. Therefore the equation for the atmospheric temperature in box i is

$$\frac{\partial \theta_i}{\partial t} = \frac{2^{\frac{R_d}{C_p^{air}}} g}{C_p^{air} P_0} \left[F_i^{top} - C_p^{water} \rho^{water} (Q_T)_i^{atm-ocean} - \frac{\kappa_{mer}}{W_i L_i} \frac{\theta_j - \theta_i}{\frac{1}{2}(L_j + L_i)} \right]. \tag{33}$$

In order to estimate the meridional heat flux we first use the Clausius-Clapeyron relation. Therefore the saturation humidity (Appendix A3),

$$q_s = C_{mer} \cdot e^{\frac{-L}{R_d T}}$$

where R_d is the gas constant for water vapor, L is the latent heat of the phase transition and C_{mer} is a constant.

The meridional fresh water flux is one of the forms used by Tziperman and Gildor (2002)

$$Q_S^{atm-ocean} = K_q \frac{\partial q_s}{\partial y} = K_q \frac{\partial q_s}{\partial \theta} \frac{\partial \theta}{\partial y} \tag{34}$$

taken at the boundary of the two atmospheric boxes. The meridional water flux is therefore proportional both to the meridional atmospheric temperature gradient (setting the strength of the synoptic eddies that carry the eddy meridional moisture flux), and the atmospheric moisture gradient (representing the difference in the ability of the atmospheric boxes to hold moisture). In this model the temperature precipitation feedback does not play a critical role as it did in Gildor and Tziperman (2001), and the variations in the meridional water flux are in the range of only $\pm 10\%$, producing relatively dryer periods during colder phases, as seen in GCM studies and in the rate of snow accumulations reconstructed from ice cores Cuffey and Clow (1997); Källén et al. (1979).

Applying this form to the atmospheric box model we get

$$(Q_S)_i^{atm-ocean} = K_q \frac{\partial q_s}{\partial \theta} \frac{\theta_j - \theta_i}{\frac{1}{2}(L_i + L_j)}$$

where K_q is chosen such that the mean meridional water transport between the two boxes is 0.7 Sv, in the range of present day values.

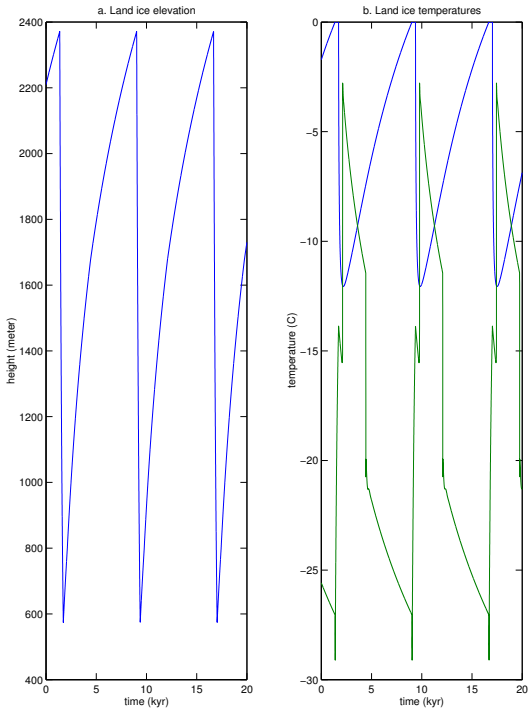

Figure 5: (a) Land ice elevation, (b) blue-basal temperature, green-temperature of the top layer of the ice

3 The mechanism

We now briefly describe the mechanism of oscillation of the land ice model, which is precisely that of MacAyeal (1993a) (section 3.1). Then we proceed in section 3.2 to describe our novel mechanism of the Heinrich event cycle, which includes the effects of ocean, sea ice and atmosphere.

3.1 The Land model relaxation oscillation cycle

During the binge (accumulation) stage, the height of the glacier grows at a rate dictated by the snow accumulation. The binge stage ends when the base temperature, heated constantly by the geothermal heat flux, has reached the melting point. Once the purge (collapse) stage begins, and sliding of basal sediment takes place, heat produced by the basal friction adds to the heat produced by the geothermal heat flux at the bottom of the glacier. The collapse stage ends when the bottom refreezes, and that happens only when the glacier's height has shrunk enough, so that the heat released by diffusion has overcome the combination of the heat created by friction and the geothermal heat flux. Once the bed has refrozen, the binge stage starts over again. Since during the purge stage the height of the glacier drops exponentially, the purge time is much shorter than the binge time, as can be seen in Fig. 5a which shows several of these relaxation oscillation cycles. Fig. 5b shows the temperature at the bed and at the top of the glacier during these cycles. The top ice temperature is influenced by the atmospheric temperature and the lapse rate (5).

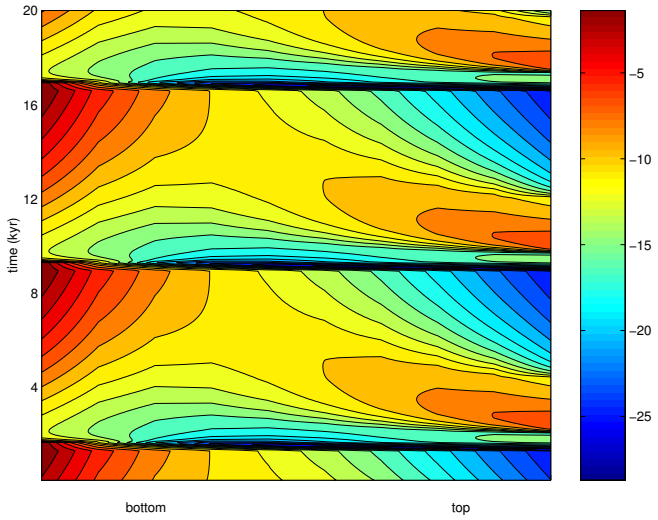

Figure 6: Temperature contour plot of land ice

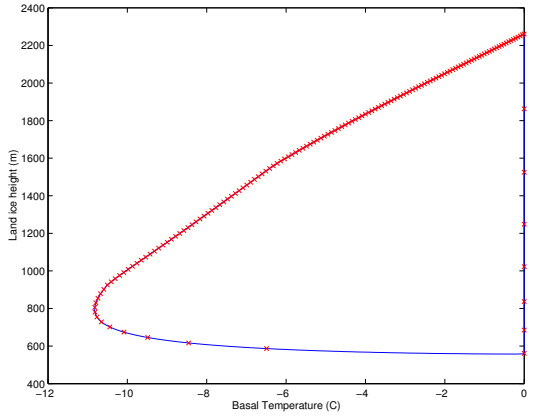

Figure 7: Hysteresis diagram of land ice growth

The temperature distribution of the land ice is shown in the contour plot of Fig. 6. The rapid changes at the top of the glacier are due to the sharp changes in atmospheric temperatures caused by the sea ice albedo (see section 3.2).

Fig. 7 shows the phase space of the height of the glacier and the bed temperature, where the red dots mark 50 year increments. It demonstrates the asymmetry of this cycle, which may be divided into three main stages. Beginning on the lower left side (point 1 on Fig. 7), the binge stage can be seen as the bottom temperature is heating. Next is the rapid purge stage, starting at point 2 on Fig. 7, as the bed temperature is constant at melting temperature. The bed doesn't refreeze immediately after a minimal collapse during this stage, because of the frictional heat. Finally, starting at point 3, the purge stops and the bed cools down until the heat begins to get trapped again, because of the insulating effect of the ice.

3.2 The proposed mechanism for the Heinrich event cycle

The above binge-purge cycle provides a mechanism for the periodic IRD layer formation but it does not explain the variations in air temperature observed over GRIP. We now present a combined mechanism of the ice sheet, ocean, atmosphere and sea ice, which can account for the missing elements. A flow chart describing this mechanism is given in Fig. 10.

We begin with conditions resembling conditions during the last glacial period. The THC is steady and so are the heat and water fluxes between ocean and atmosphere. The land ice sheet is located at 60N with an area of 1 million sq. km., which represents the ice sheet over Hudson Bay. There is also a sea ice cover of close to 80% of the northern box ocean area. The land ice grows (Binge stage), and we refer to this stage as quasi equilibrium #1.

The ice sheet grows at a rate dictated by snow accumulation. When the purge stage of the land ice sheet begins (year 1300, Figs. 8,9), large fluxes (0.1-0.25 Sv, matching estimates of Alley and MacAyeal (1994)) of fresh water are discharged into the Northern Atlantic (box 2). This rapid discharge of fresh water immediately reduces the salinity in box 2, and therefore also the density. The decrease in density in box 2 slows the THC which is governed by the two density gradients $\rho_2 - \rho_1$ and $\rho_3 - \rho_4$ (15). Since the later changes rather modestly, the main contribution at this stage to the change in the THC is due to the drop in ρ_2.

Early in the purge stage, the slowing down of the THC reduces the warm water flow into the northern upper box, resulting in a cooling of the SST of the upper northern waters (T_2, temperature of box 2). This cooling then leads to a rapid buildup of sea ice, and T_2 is further cooled by the atmosphere above it which gets colder due to the sea ice albedo effect. As the sea ice grows the effect of the atmosphere on the ocean decreases, due to the insulating effect of the sea ice. Eventually advection and diffusion from neighboring boxes overcomes the reduced atmospheric cooling. This slows down the creation of sea ice, resulting in a new quasi-equilibrium of the sea ice at about 90% of the box area.

Why does the system settle in such an equilibrium? Suppose the sea ice extent grows. Then the insulation between ocean and atmosphere would grow as well and box 2 would be heated by box 1 while receiving less cooling from the atmospheric box. This will result in an increase in T_2, melting of sea ice, and therefore in a return to the equilibrium state. An initial reduction of the sea ice will cause insulation to decrease, T_2 will be cooled by the atmosphere forming more sea ice, and back to equilibrium.

Now the system is at its second quasi equilibrium state (with 90% sea ice - year 1350-2000 Figs. 8,9). The THC is low (at 6 Sv due to the condition described in section 2.2) so that the diffusive processes are relatively dominant over the advective processes. T_4 therefore increases due to diffusion from the warmer upper mid-latitude box 1, and diffuses into box 3 increasing T_3.

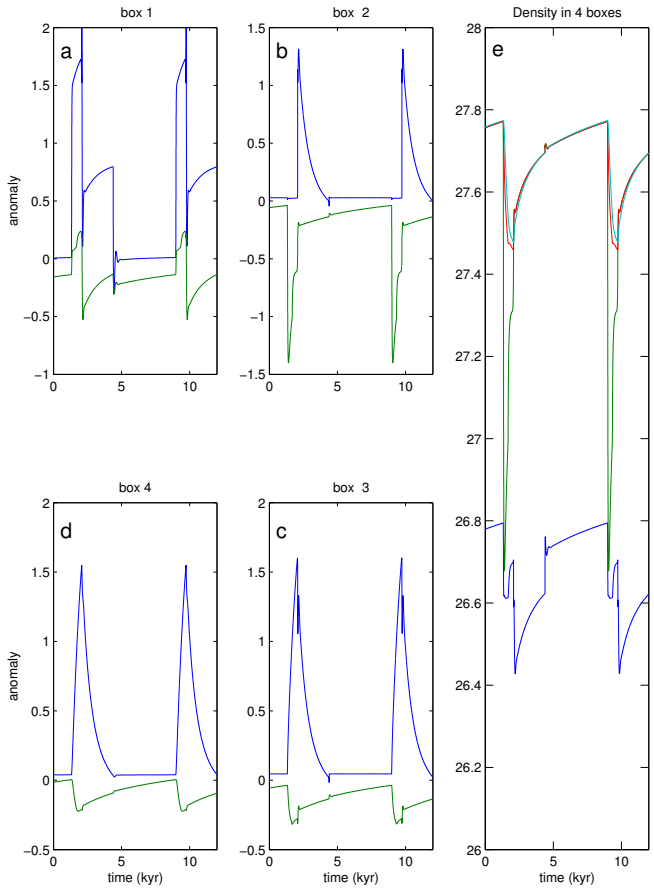

Figure 8: (a-d) Temperature anomalies (blue) and Salinity anomalies (green) for the four ocean boxes. (e) Density for the four boxes, 1-blue, 2-green, 3-red, 4-turquoise

During this time the salt diffusion from the higher salinity boxes 1 & 3 into box 2 continues, and eventually the diffusive salinity flux increase overtakes the reduction in salinity due to the fresh water flux from the collapsing glacier and S_2 begins to increase.

When the purge stage stops (year 1650, Figs. 8,9), the fresh water input from the land ice into box 2 stops as well and S_2 increases more rapidly, consequently increasing ρ_2 and the THC. This is a positive advection feedback process Marotzke et al. (1988), since the strengthening of the THC increases the advection from saline box 1 into box 2, increasing its density and resulting in a stronger yet THC. The THC strengthening also cools T_1 rapidly and heats T_2 resulting in gradual (but with an increasing rate due to the positive sea ice albedo feedback) melting of sea ice. Thus the melting of sea ice brings an increase in the atmospheric temperature over the melted sea ice (atmospheric box 2). The beginning of the melting of the sea ice marks the end of quasi equilibrium #2.

At this stage the density of box 2 is increasing fast, while ρ_3 is decreasing due to the continued heating of T_3 by diffusion, and decrease in S_3 due to diffusion from the low salinity box 2. Once ρ_2 reaches ρ_3, convection begins (year 2150, Figs. 8,9). The convection in the northern ocean boxes

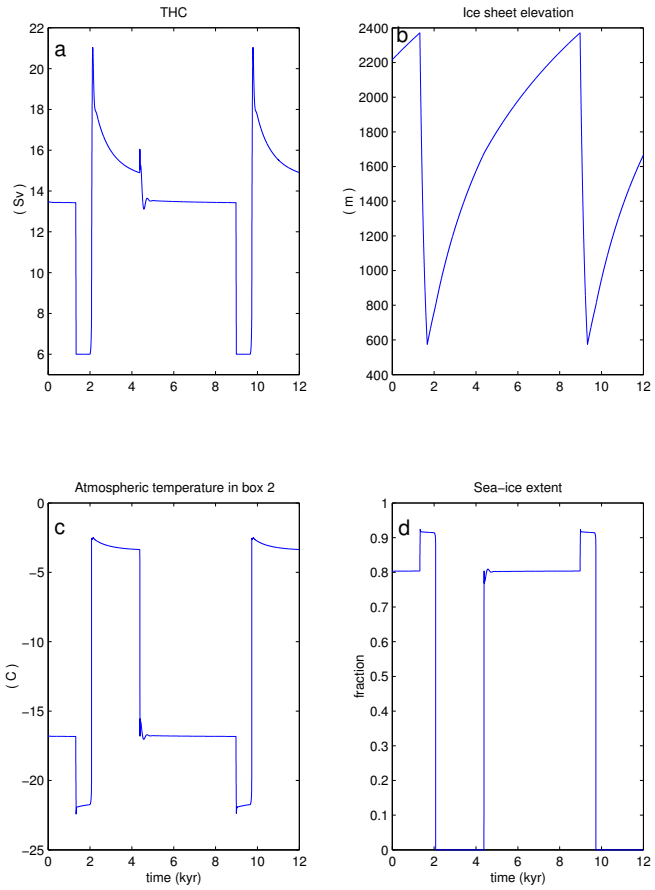

Figure 9: A full Heinrich Event cycle. (a) THC, (b) Land-ice elevation, (c) Atmospheric temperature in the northern box, (d) Sea-ice extent in the northern box

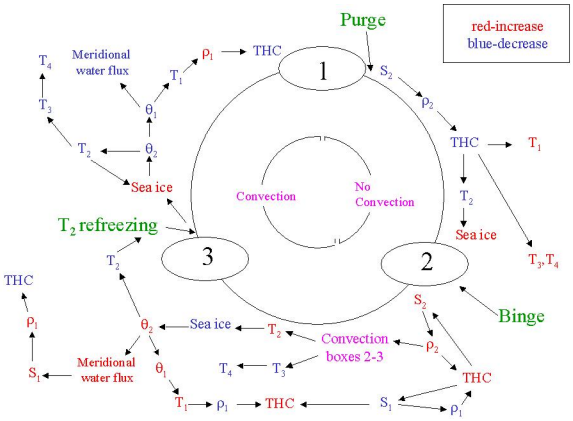

Figure 10: A flow chart of the new mechanism, red labels denote increase and blue labels denote decrease.

means immediate heating of the upper box by the warm lower box. This rapid heating cannot be balanced by the colder atmosphere, and rapid sea ice melting begins. The salinity also increases rapidly in box 2 due to the convective mixing with box 3. Thus increasing ρ_2 and amplifying the positive advective feedback.

The sea ice looses volume quickly, resulting in rapid increase of air temperature because of the sea ice albedo effect. This increase in atmospheric temperature in atmospheric box 2, increases also the temperature in atmospheric box 1 through the meridional heat exchange of the atmosphere. As a result the air-sea heat flux grows rapidly, and T_1 is heated (peak of T_1, Fig. 8 year 2100). This amplified process settles toward equilibrium once the sea ice extent reaches zero.

The rapidly growing THC increases ρ_2 and decreases ρ_1, increasing the THC to high values. Also, as convection starts ρ_2 and ρ_3 equalize quickly, while it takes the larger box 4 longer to respond, creating for a short period an ineligible difference $\rho_3 - \rho_4$. This delayed response of the deep ocean also intensifies the THC peak seen in Fig. 9 (year 2150). The system is now in its third quasi equilibrium state of zero sea ice (years 2100-4300, Figs. 8,9).

Due to the insulating effect of sea ice, once the sea ice is gone, T_2 is strongly cooled by the atmosphere, and after its rapid increase due to convection, T_2 begins to decrease (year 2150, Fig 8). The convection with cold box 2 causes T_3 to decrease rapidly, and this cooling continues as well while T_2 is cooling. The growing THC increases the advection and T_4 cools as well via advection from box 3. The gradual decrease of T_2 also cools the atmosphere above it due to the high level of atmosphere-ocean interaction when no sea ice is present.

The rise in atmospheric temperature in both atmospheric boxes, intensifies also the atmospheric meridional fresh water flux (34), therefore causing S_1, thus ρ_1 to rise. This process acts as a break for the intensification of the THC, and after the peak in the THC (year 2150 Fig. 9) due to the deep ocean delay discussed above, the THC begins decreasing.

The box temperatures T_2, T_3, T_4 are now decreasing, and the system remains in this state until T_2

Eq. #	Duration	Sea ice	Main Processes	Ending Trigger	Convection
1	4300 yr	80%	Building land ice	Purge	On
2	700 yr	90%	Heating of boxes 3,4, due to diffusion Drop in S_2 due to land ice input	Binge & growing THC	Off
3	2200 yr	0	High THC, Cooling of box 2, High atmospheric temperature	$T_2 < T^{si}$	On

Table 4: Summary of the three quasi equilibrium states

decreases below the sea ice freezing temperature. The salinity is slightly rising in boxes 2,3,4 due to the land ice buildup. Once sea ice forms (year 4300 Figs. 8,9), the temperature in atmospheric box 2 cools down due to the albedo effect of the sea ice, this decreases T_2 more, intensifying this process, creating a positive feedback. Within 10 years the sea ice is back to 80% of box 2, and the atmospheric temperature is cooled back to glacial time values. The positive feedback cooling of box 2 stops as in quasi equilibrium #1 because of the insulation of the sea ice and T_2 sets into equilibrium (year 4400, Figs. 8,9). As a result, the temperatures T_3 and T_4 set in equilibrium as well (in this order), and the delayed response of the deep ocean creates the second smaller peak of the THC (year 4400, Figs. 8,9). This marks the termination of the high THC.

During the transition back to quasi-equilibrium #1, T_1^{atm} also cools down through the meridional heat flux of the atmosphere, decreasing T_1. This sharp drop in T_1 triggers a rise in ρ_1, and reduces the THC back to its initial level of equilibrium #1. Eventually T_1 balances as a result of the balance of the three other boxes initiated by the sea ice equilibrium. The cycle is now complete, the system has settled to the conditions of quasi equilibrium #1 (years 4700-9000, Figs. 8,9), until the next purge. Table 4 summarizes these three quasi-equilibrium states.

We can make another distinction between the three quasi equilibria. Equilibrium #1 is stable in the sense that all the dynamical parameters of the coupled ocean-atmosphere model are stable and without the fresh water pulse from the next purge they would have remained in this equilibrium. This is not the case in equilibria #2 & 3, though the sea ice is in balance, the ocean and atmosphere dynamical variables are changing in time and the time it takes the system to get out of these states depends only on the time it takes these dynamic variables to reach the point in which the sea ice balance breaks. A useful way to view these three quasi equilibrium states, is in the hysteresis diagrams in Fig. 11. In Fig 11a we present the phase space of the THC vs the density of box 3, this

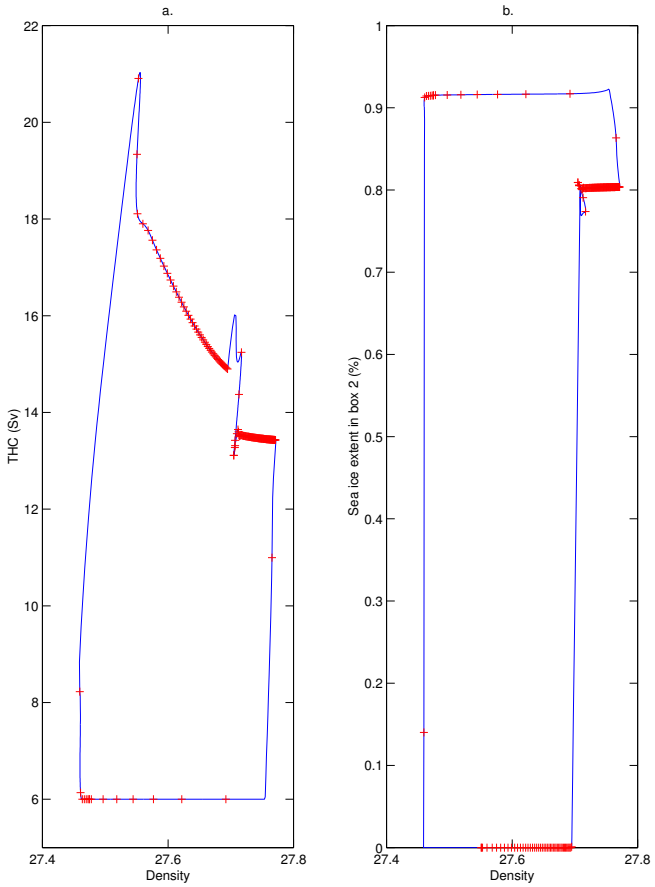

Figure 11: (a) Hysteresis diagram of the phase space of the THC and the density in box 3, (b) Hysteresis diagram of the phase space of the sea ice extent and the density

hysteresis diagram's direction is clockwise. In Fig 11b the phase space of the sea ice extent and the density in box 3 is presented, while this diagram's evolution with time is counterclockwise. Every red dot represents a time increment of 50 years.

3.3 Discussion

Although this clearly is a very simplified model it seems that it may have demonstrated quite an interesting mechanism. As the purge stage advances, diffusion of salt from other parts of the ocean must have grown because of the growing density differences. IRD and other proxy evidence show that the purge ended rather abruptly as implied in our model. This rapid end of fresh water supply and growing diffusion could have created a counter effect to the initial slow down of the THC, and ignited a strong advective feedback mechanism which enhanced the THC. The strengthening of the THC and the diffusive heating of the deep ocean, cause the convection in the northern ocean which triggers the sea ice breakdown, and the albedo effect brings the rapid growth in atmospheric temperatures that we view in the GRIP data Dansgaard et al. (1993). The time scales

in our model (although depending on model parameters, see section 5), seem to match well the observed ones. The convection, which causes the atmospheric heating occurs 750 years after the initial purge, which is in average the corresponding timescale found when comparing the GRIP records and the IRD records. This rapid increase in atmospheric temperatures is followed by a gradual decrease in atmospheric temperatures, also matching the GRIP data. The warm period lasts several thousand years after which the atmosphere and ocean gradually settle back to the initial equilibrium conditions.

4 Synchronized collapses

We now wish to address the second main objective of this study, which is a proposed mechanism for the synchronous collapse of ice different sheets during Heinrich events.

We now first explain what sets the frequency of Heinrich events of a given ice sheet, and then explain how the interaction between two such ice sheets can still make them oscillate at the same frequency. Beginning with the first issue, note that in MacAyeal (1993b) the 7 kyr relaxation oscillation cycle was demonstrated using a fixed specified average sea level temperature and a specified adiabatic lapse rate, which were specified as the upper boundary conditions of the ice sheet. The period of these oscillations is quite sensitive to this temperature boundary condition. In our model the upper boundary condition is given as linear interpolation of the temperature of the two atmospheric boxes, depending on the location of the ice sheet. Therefore the choice of the location of the ice sheet influences the frequency of the oscillation (Fig. 12), although the atmospheric temperature is determined also by the atmospheric meridional heat flux and by the temperatures of the surface ocean boxes. A second parameter which distinguishes in our model between ice sheets is the area of the ice sheet. The area determines the amount of fresh water discharge of the ice sheet into the ocean, and therefore its effect on the ocean circulation and on the coupling mechanism. In our standard run, the ice sheet is set at 60 N and has an area of 10^6 sq. km..

Two such glaciers placed at different latitudes would therefore oscillate at different frequencies. However, since both affect the ocean via their fresh water fluxes, and both are affected by the same atmospheric temperature we may expect them to synchronize. We therefore insert into the model a second ice sheet representing a "European" ice sheet such as the Icelandic, Fennoscandian or British ice sheets (which are all much smaller than the LIS).

The first case we examine is of two ice sheets located at the same latitude. The initial height of the two ice sheets is different, this also determines the initial temperature distribution, meaning the two ice sheets are initially out of phase. The binge-purge relaxation oscillation of two coupled ice sheet, where the small one is 1/8 the area of the larger one is presented in Fig. 12a. The

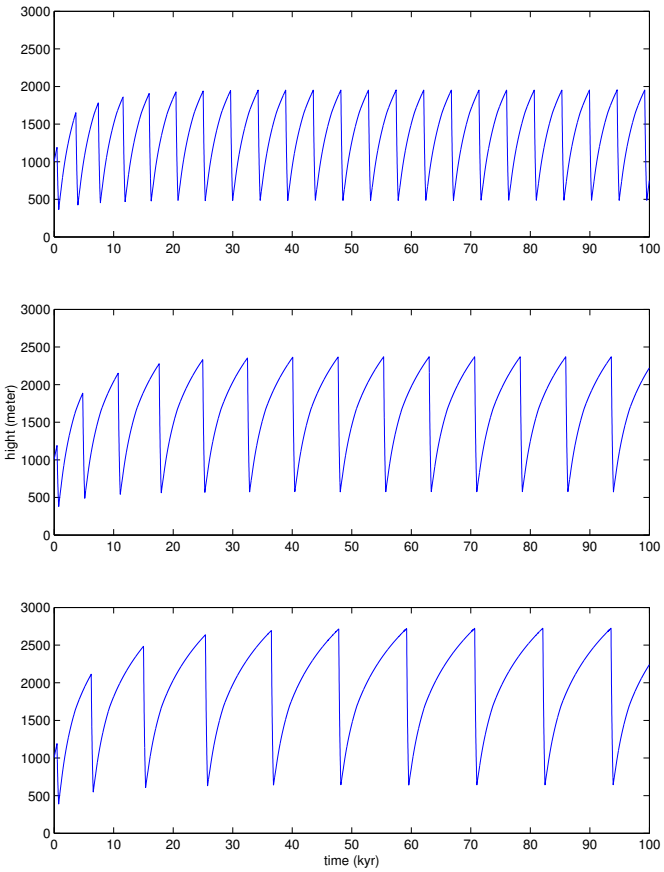

Figure 12: The dependence of the upper boundary temperature in the land ice sheet. The upper, middle and lower graphs correspond to latitudes of 57,60 and 63 respectively.

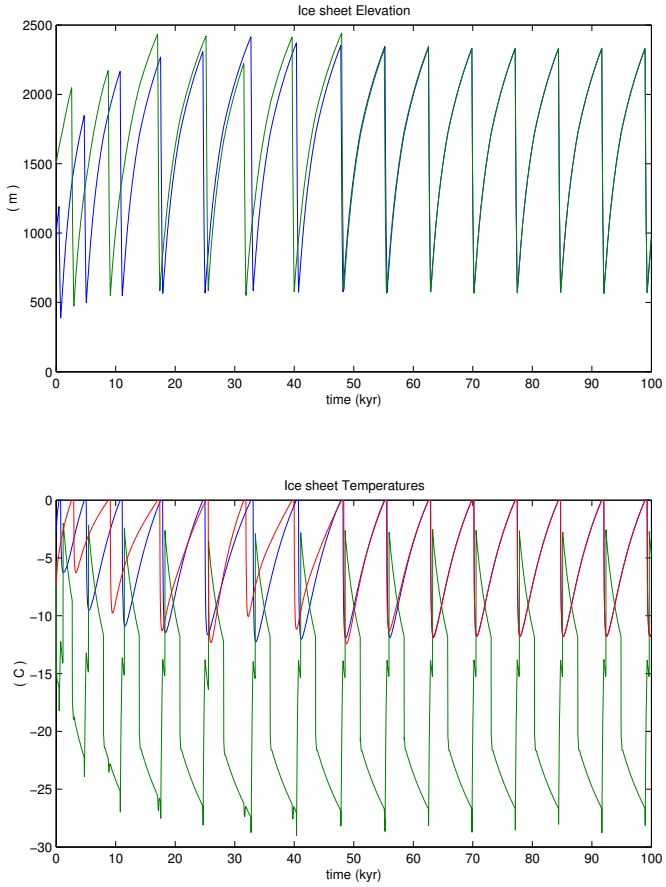

Figure 13: (a) Phase locking between two ice sheets, one with an area of 10^6 sq. km. and the other 1/8 this size. (b) The ice sheet temperatures, blue and red are the basal temperatures of the two ice sheets, the green curve is the atmosphere temperature at top of the bigger ice sheet.

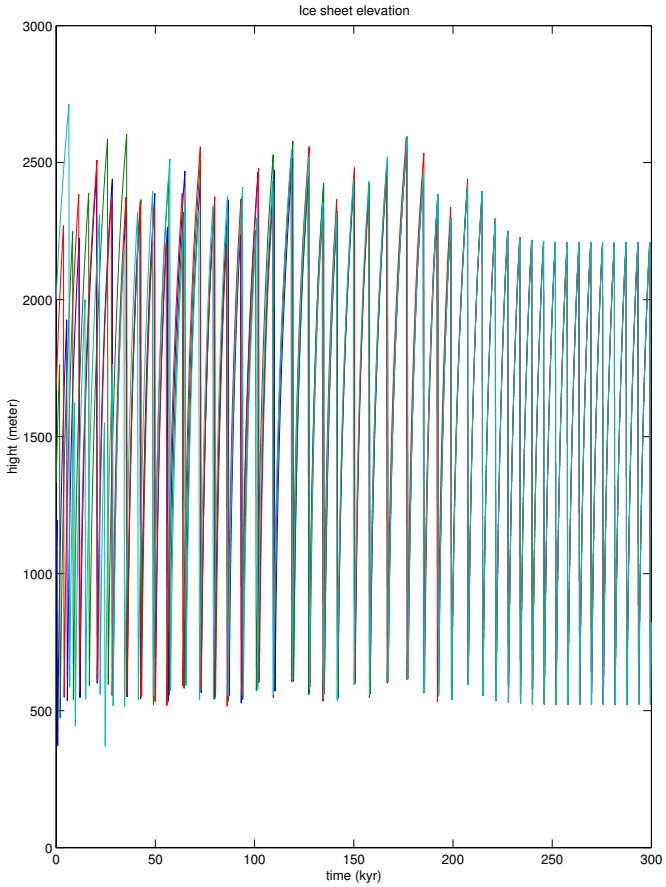

Figure 14: Phase locking between four different size ice sheets, all at the same latitude. (This graph has been done with a slightly different set of parameters)

larger the area of the ice sheet the bigger impact it will have on the ocean circulation, though we find that adding a second ice sheet of up to 1/2 the size of the larger one, still maintains the mechanism presented above. Nevertheless we find that taking the second ice sheet to be relatively big compared to the first one may cause a longer time until phase locking is observed. Fig. 12b shows how the ice sheet temperatures vary until the ice sheets become phase locked. It can be seen that the atmospheric temperature (influenced mainly by the bigger ice sheet) in the transition from the purge stage to the binge stage, determines the base temperature profile for the smaller ice sheet and therefore the timescale of the cycle.

The coupling of glaciers can be done for more than two glaciers, as in seen Fig. 14 where we couple four different size ice sheets.

Next we set one ice sheet at 60N, and vary the latitude for the other ice sheet. Our first test is to see how wide is the latitude range in which we find a 1:1 phase locking. Fig. 15 shows an example of binge-purge oscillator plots for two glaciers, one at 60 N and the second at 58 N, where the second one is 1/4 the area of the first one. By analyzing the different runs we find that a smaller ice sheet, whose period when oscillating by itself, is 40% shorter, or 10% longer in frequency, is

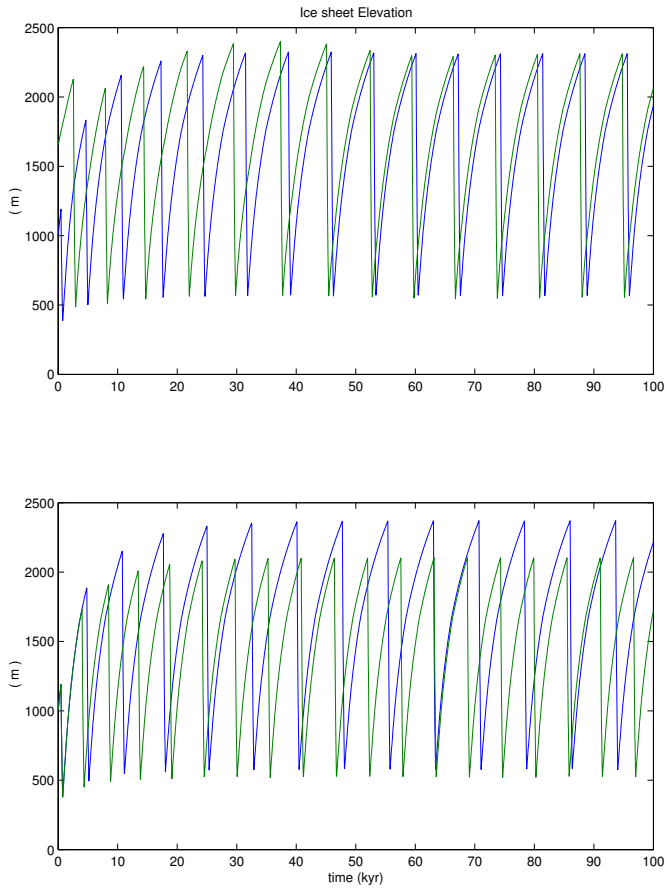

Figure 15: upper: Coupled binge-purge oscillations for two ice sheets, one at 60 N and the second at 58 N. lower: Self frequencies of a one ice sheet model corresponding to both latitudes.

1:1 phase locked to the larger (forcing) ice sheet. Also generally the larger the second ice sheet, the larger is this range. Ice sheets that had initially closer independent frequencies have less phase difference when phase locked, as can be seen by comparing Figs. 13 and 15. Fig. 15b shows the frequency of the oscillations as if each of the ice sheets would have oscillated independently.

When we place the smaller ice sheet southward we find higher order phase locking. In Fig. 16 2:1 and 2:3 phase locking is presented. Noting that a glacier on the European side feels a warmer atmospheric temperature than a glacier from the same latitude on the American continent, we realize that European ice sheets would tend to oscillate faster even at the same latitude. Therefore the higher order phase locked glaciers may represent glaciers such as the Icelandic or the Fennoscandian although they are northward than the LIS. This brings us to hypothesize that the mechanism behind the D/O events may have been some high order phase locking (3:1) between the forcing LIS and the smaller Icelandic Bond and Lotti (1995) or Fennoscandian ice sheets Fronval et al. (1995).

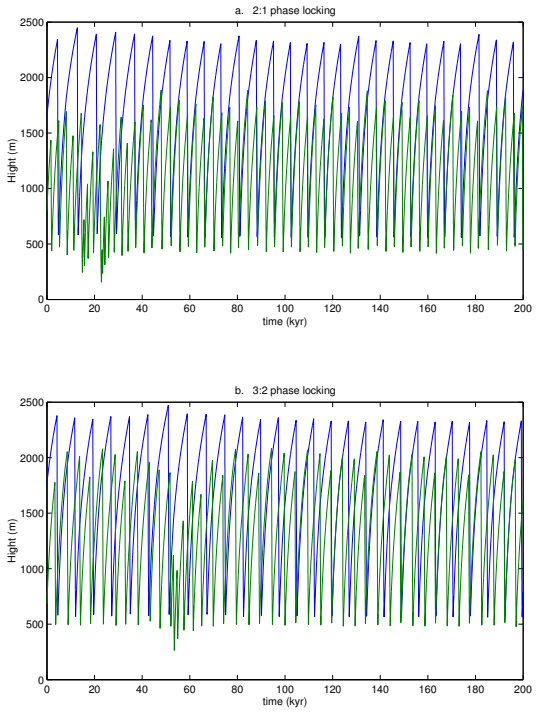

Figure 16: a. 2:1 phase locking between our standard Ice sheet and an ice sheet 1/4 in size and "at" 55.5 N. b. 3:2 phase locking between our standard Ice sheet and an ice sheet 1/4 in size and "at" 56.4 N. Both plots are presented here 40 kyr after the beginning of the run.

5 Parameter Sensitivity

In order to gain a better understanding of the physical mechanism presented and its dependents on the model parameters, we preform a series of sensitivity tests, devoting a subsection to each parameter. We use several strategies of sensitivity analysis. The first is to simply vary a single parameter. The second strategy is to vary a certain physical quantity in our model, such as the strength of the THC, which may depend on several parameters. Another strategy we used is to vary a certain parameter and try to compensate for this change by varying other parameters as well, in order to maintain our physical mechanism.

Very often we find that significantly varying a single parameter, shifts our model into a different regime than the one we wish to study here. However, in all such cases we find that we can compensate by changing other model parameters and return to the regime showing the Heinrich event mechanism discussed above. We thus conclude that this mechanism is robust and occupies a significant volume in our multi dimensional parameter space.

5.1 THC

As explained in section 2.2 the THC amplitude is determined by the horizontal density gradients, and has a lower bound at 6 Sv. This barrier is set because we believe that the THC has not been shut down completely Legrand and Wunsch (1995) during the last glacial period. Nevertheless this limit is not essential for our mechanism and when applying only a the linear horizontal density gradient (15) to determine the THC, our mechanism does not change considerably (Fig. 17). Without the lower bound the THC goes down to -2 Sv (i.e. reverse) after the purge, but the main characteristics of the mechanism remain the same.

This sensitivity test is divided into two parts. In the first part we present the results without the 6 Sv barrier, where the diffusion coefficients and meridional heat flux are tuned in order to compensate for the heat loss due to less advection. The main characteristics of the model are compared with and without the barrier and with different mean THCs in Fig. 17. Also the choice of a mean THC of 13.5 Sv represents the THC that is generally believed to be somewhat weaker than at present day. Any other value between 10-18 Sv will give us the same mechanism.

The second test we did is to change only the coefficient C_u from the friction term in the horizontal momentum equation. We varied this factor while leaving the horizontal diffusion coefficients and meridional heat flux coefficient fixed. As can be seen in Fig. 18, the increase in the influence of advection compared to diffusion increases the time of zero sea ice. This happens because the higher THC increases the warm water transport between boxes 1 and 2, therefore it takes box 2 longer to reach the freezing point during quasi equilibrium stage #3. In Fig. 18 a case with a long period without sea ice is shown, where the three characteristics presented: THC, sea ice extent and the temperature of box 2, are the three most effected by the variation of this parameter, it is seen that the mechanism and the total period do not change only its partition between quasi equilibriums #1 and #3.

5.2 Ocean Diffusion coefficients

The model uses one standard horizontal diffusion coefficient for both the upper and deep ocean horizontal diffusion, and another coefficient for the north and south vertical diffusivities.

More or less diffusion may be compensated by variations in other horizontal heat transports mechanisms such as advection and atmospheric meridional heat flux as explained in the discussion of sensitivity to the THC (Fig. 17). Therefore we now vary only the diffusion coefficient.

In our three state mechanism the main role of vertical diffusion is the heating of box 4 by box 1, which begins after the purge and ends when convection begins (section 3.2). Therefore we see a rise in T_4 that follows increase of the vertical diffusion parameter. This increase also increases T_3 and T_2 respectively, and therefore increases the length of quasi equilibrium # 3. Decrease of the

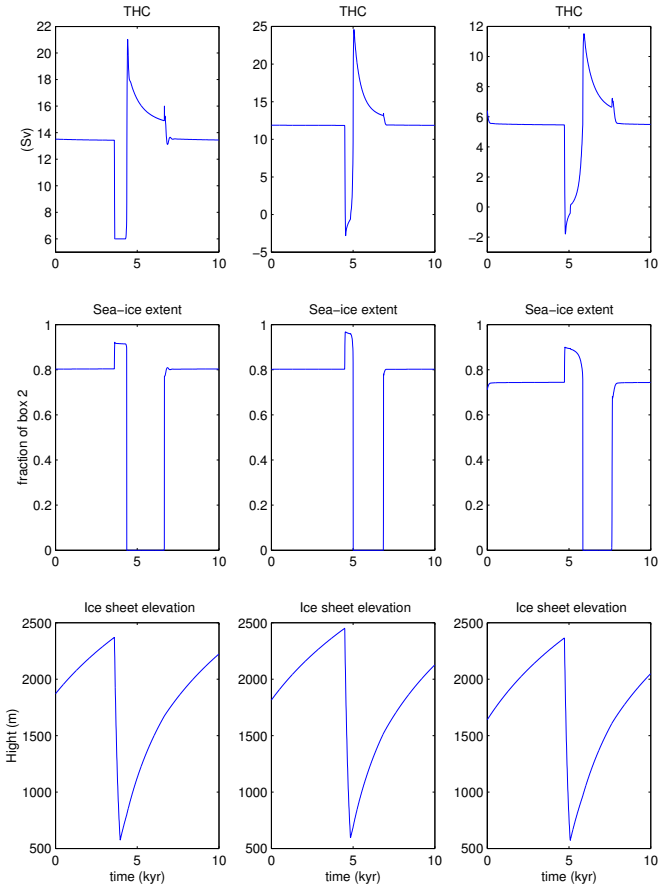

Figure 17: Sensitivity to THC: Three similar runs presenting the THC, sea ice extent and ice sheet elevation, giving three different mean THCs. On the left our standard run with mean THC of 13.5, where the 6 Sv barrier is applied to the linear horizontal density gradient (15), in the middle a mean THC of 12 Sv without the 6 Sv barrier and on the right a mean THC of 5.5 Sv also without the 6 Sv barrier. These results show that our proposed mechanism is not dependent on the strength of the THC.

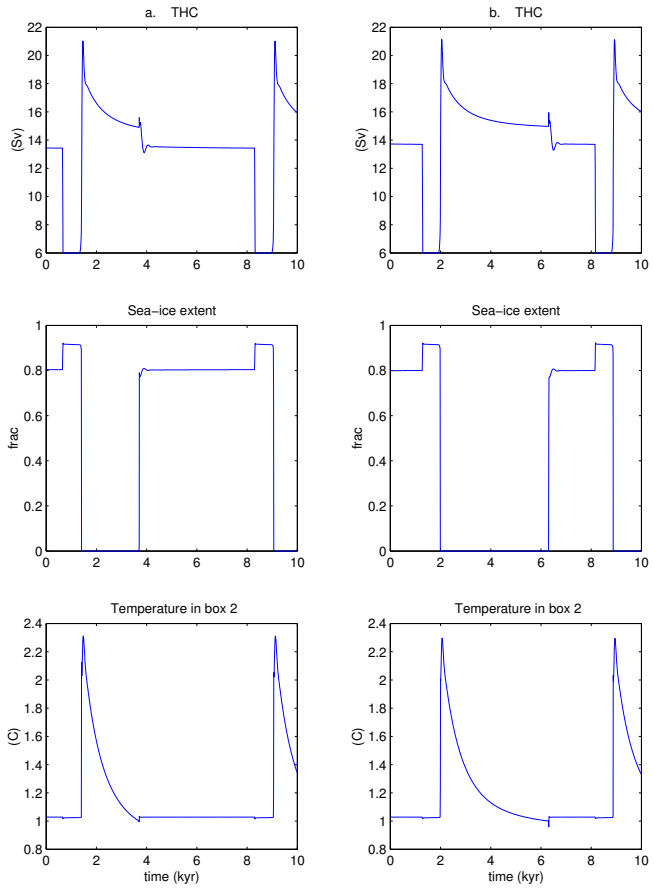

Figure 18: Sensitivity to C_u: Three characteristics of the cycle, the THC, sea ice extent and T_2. On the left they have the original value of C_u, and on the right it is greater by 2%. All other parameters are not changed.

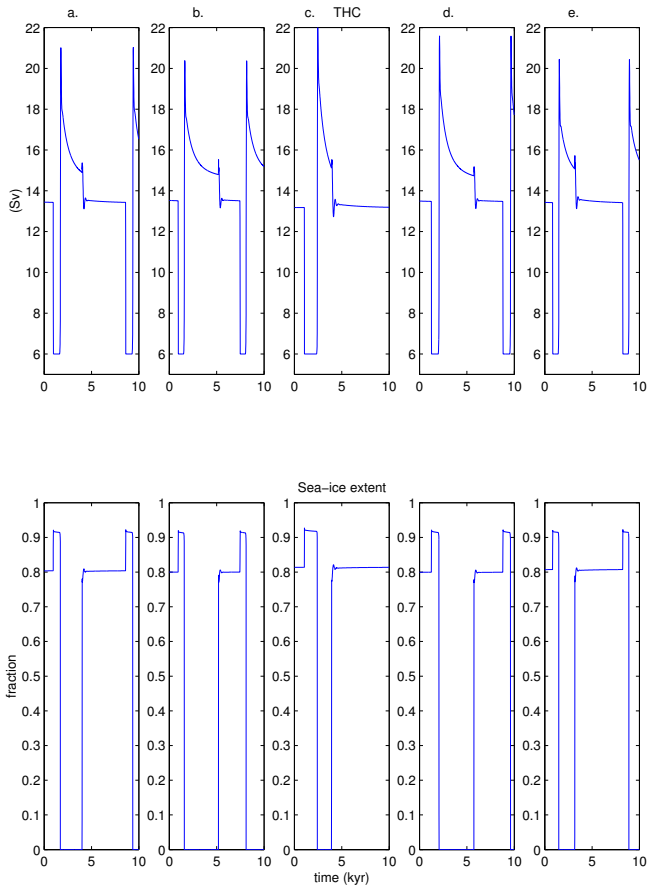

Figure 19: Sensitivity to the horizontal and vertical ocean diffusion coefficients (κ_h, κ_v);
THC and Sea ice extent for different runs: a. standard run, b. +4% in horizontal diffusion, c. -10% in horizontal diff., d. +20% in vertical diff., e. -20% in vertical diff. Other parameters have not been changed.

vertical diffusion coefficient has the opposite effect. Results of twenty percent variations in both directions are presented in figure 19.

Increase of the horizontal coefficient transfers more heat from box 1 to box 2 after the purge stage, thus reducing the temperature of box 1, so less heat is diffused vertically to box 4, similar to the effect of reducing the vertical diffusion coefficient. This increase also transfers more heat to box 2 during quasi equilibrium # 3, increasing the length of the no sea ice period. Also, increasing this parameter results in more diffusion of salt during quasi equilibrium # 2, thus shortening this equilibrium state which ends when ρ_2 overcomes the limit which enables the positive advection feedback, (section 3.2). Increase in this parameter also causes atmospheric box 2 to be warmer, thus creating warmer conditions for the ice sheet resulting in a shorter binge stage and a shorter overall cycle. Fig. 19 presents variations in the horizontal diffusion coefficient.

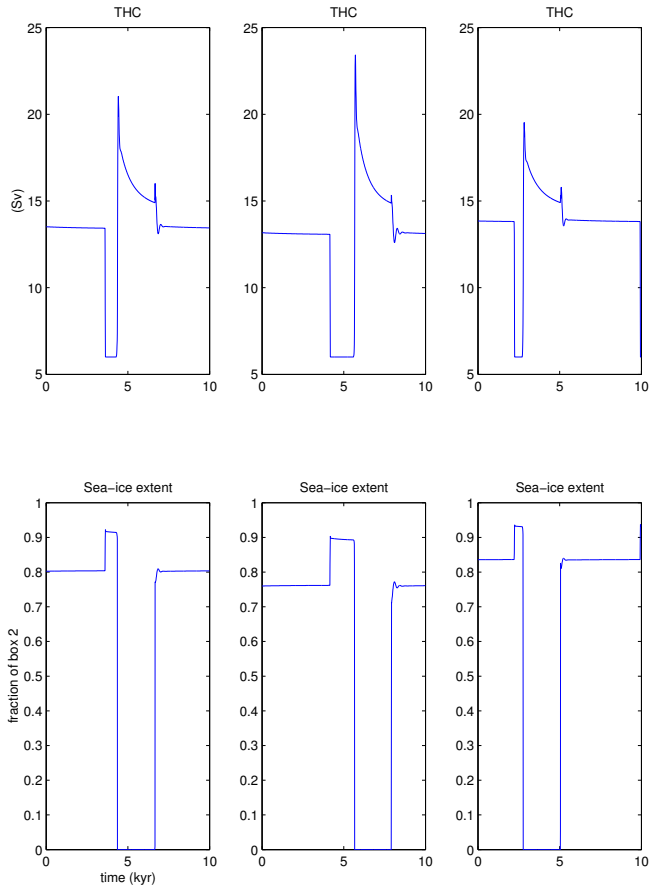

Figure 20: Sensitivity to sea ice albedo: The THC and Sea ice extent presented for three different sea ice albedo's; left: our standard run with 0.55, middle: 0.45, right: 0.65. Other parameters have not been changed.

5.3 Energy balance parameters

We now examine the sensitivity to parameters that influence the atmospheric energy balance: the shortwave radiation, the emissivity and the albedo coefficients. The incoming shortwave solar radiation, is the average energy entering each box. The long-wave emissivity coefficient in the atmosphere model, P_{lw}, represents factors such as cloud cover, humidity, and atmospheric concentration of aerosols and CO_2, and is different for each atmospheric box (29). The albedo coefficients which determine the amount of shortwave reflected out of the atmosphere, are taken as very rough average values from Trenberth (1992). The only parameter of all that plays a major dynamical role is the sea ice albedo, due to the strong sea ice albedo feedback (see section 3.2). As all other dynamical variables, large changes in sea ice albedo can be compensated with other elements of the model, we experimented with this parameter and the results can be seen in figure 20. Increasing this parameter causes a colder atmosphere over the sea ice resulting in a bigger sea ice extent and a shorter quasi-equilibrium #2 stage (see 5.4 for a more detailed explanation).

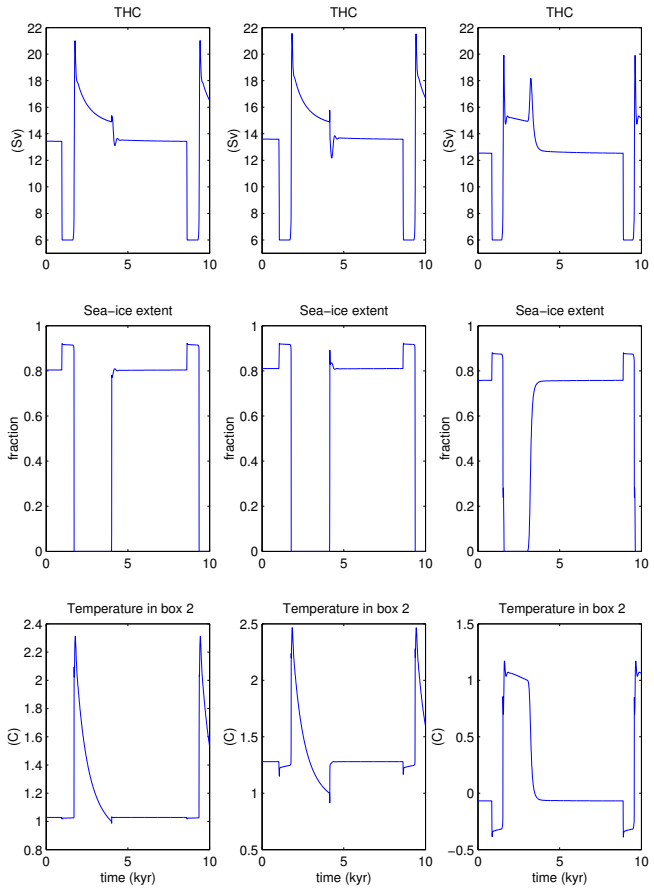

Figure 21: Sensitivity to the sea ice parameters, shortwave parameter and typical timescale. left: 25% and 1 year, middle: 25% and 10 years, right: 50% and 10 years. Other parameters have not been changed.

5.4 Sea ice parameters

The parameter P^{seaice} determines the percentage of melting of sea ice directly from shortwave radiation Maykut and Perovich (1987). As explained in section 2.2.1, the components of sea ice growth balance each other when in equilibrium, thus more melting of sea ice from the shortwave component means a lower temperature of box 2 during sea ice equilibrium (quasi equilibrium # 1). Therefore by varying this parameter we only change the balance between the different contributions to sea ice growth/melting. A larger value of shortwave melting of sea ice also changes the growing rate of sea ice after quasi equilibrium #3 as seen in Fig. 21.

Since meridional variations in the sea ice extent are very large we use a large typical timescale of one year $\tau^{seaice-ocean}$ in (20). This parameter has almost no influence on the mechanism, and the effect of changing this parameter to 10 years or 1 month is negligible. A short time scale will force T_2 in equilibrium to be very close to the freezing temperature because of the strong effect of the variation between T_2 and the sea ice freezing temperature. A larger time scale will of course increase the sea ice buildup/melting rate as can be seen in Fig. 21.

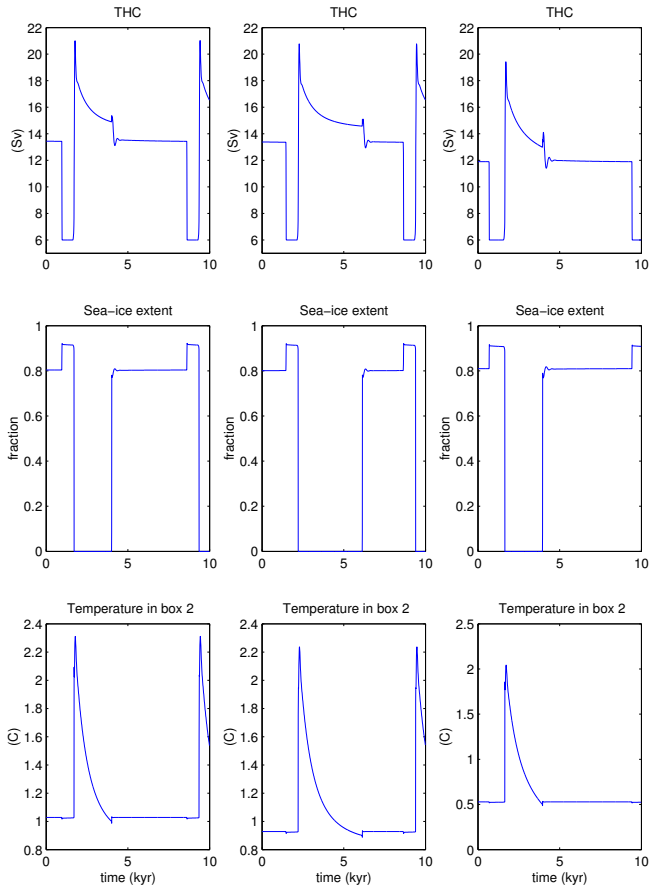

Figure 22: Sensitivity to the sea ice freezing temperature (T^{seaice}): The THC, sea ice extent and T_2 presented for three runs; left: freezing temperature of 1 C, middle: freezing temperature of 0.9 C, right: freezing temperature of 0.5 C with a reduction of 6% in C_u for compensation.

The third sea ice parameter we examine here is the sea ice thickness, for which we use a standard thickness of 2 meters as observed today in the Arctic. Varying this parameters to 4 meters has very slight, if any, effect on the model.

The freezing temperature of sea ice is an important parameter since it triggers the creation of sea ice (section 3.2). Since it is an average over the entire box this parameter is chosen above the freezing temperature of sea water (1 C instead of -2 C). In figure 22 it is demonstrated how a small variation in this parameter effects the mechanism, but varying other parameters related to the heat flow into box 2 (such as C_u) can compensate for this effect. Therefore although the important role of this critical temperature its choice does not effect the mechanism.

5.5 Atmospheric meridional heat transport

The meridional atmospheric heat flux is determined by the parameter κ_{mer} in (32). By increasing κ_{mer} we heat the atmosphere of box 2 and cool the atmosphere in box 1, which also cools T_1. This

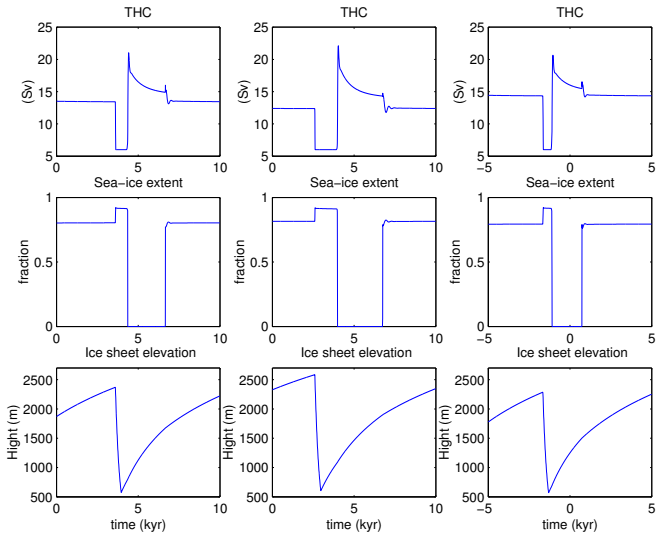

Figure 23: Sensitivity to κ_{mer}: The THC, sea ice extent and land ice height presented for three different κ_{mer} values; on the left is our standard run, in the middle +10%, and on the right -10%. Other parameters have not been changed.

increases ρ_1, resulting in a weaker THC, so it takes the system longer to recover from the purge. Fig. 23 shows an example for a variation of $\pm 10\%$ in the meridional heat flux in comparison to our standard run.

5.6 Ocean-Atmosphere heat flux

The heat transport between ocean and atmosphere is determined by the specified timescale of air-sea interaction ($\tau^{atm-ocean}$). The time scale for the rate of heating of the upper ocean is determined by the depth of the mixed layer. A typical time scale is of 30 days per 50 meters mixed layer depth. In our model, the upper layer which interacts with the atmosphere is 400 meters deep. Since some of this depth range represents stratified fluid with slower mixing time scales, we use a restoring time of 4 years. We now vary this parameter (assuming stronger mixing), and the model results for a restoring time of 1.8 years are presented in Fig. 24. It can be seen that the main difference from our standard run is that due to the stronger atmosphere-ocean interaction the ocean is colder and therefore sea ice extent during quasi equilibrium # 1 is higher. Also due to the stronger coupling of the upper layer to the atmosphere, quasi equilibrium # 2 & 3 are shorter, and the delayed response of the deep ocean is amplified (the higher second THC peak).

5.7 Ocean-Atmosphere fresh water flux

The meridional atmospheric water flux is determined by (34). Increasing K_q causes a higher accumulation rate during the binge stage, therefore a larger height. Due to the lapse rate, the top of

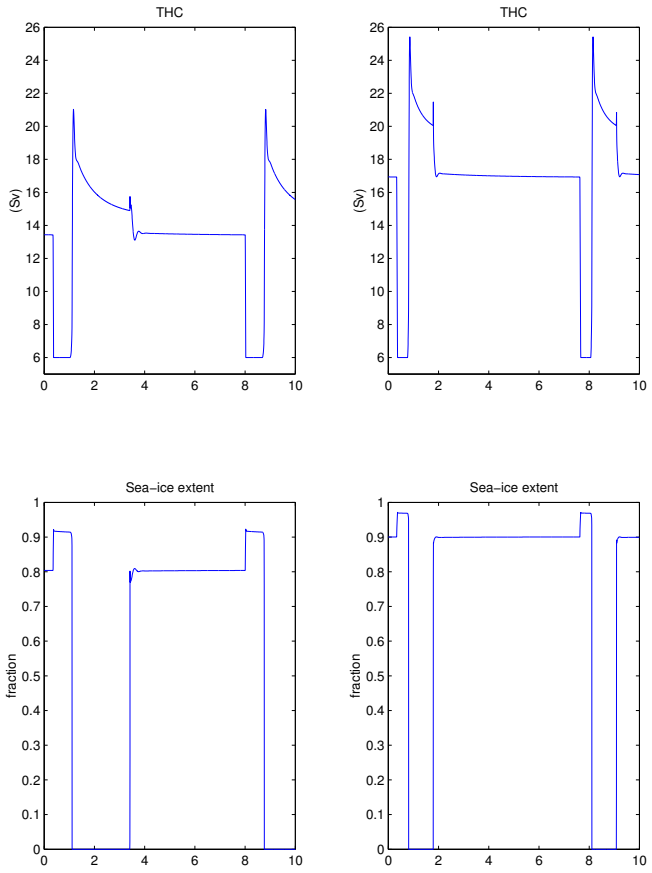

Fig. 24: Sensitivity to typical timescales of ocean-atmosphere interaction ($\tau^{atm-ocean}$): On the left: 4 years, on the right: 1.8 years.

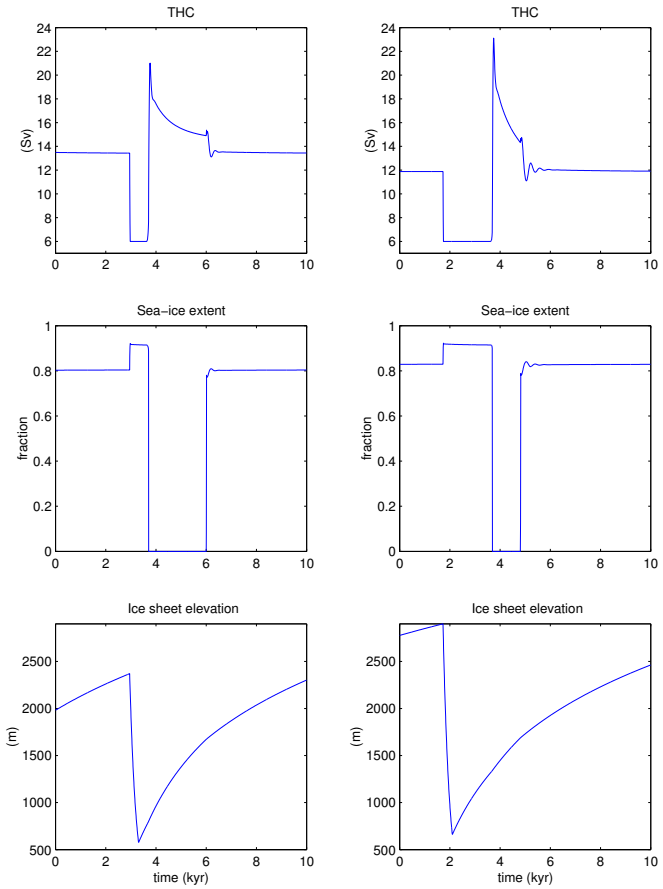

Figure 25: Sensitivity to K_q :The THC, sea ice extent and land ice height presented for three different runs; On the left is our standard run, and on the right K_q is greater by 4%. Other parameters are not changed.

the ice sheet is colder, resulting in a longer time before the ice sheet bottom temperature condition allows the purge to begin. This also creates a stronger discharge of fresh water during the purge (because of faster accumulation during binge). More fresh water flux from the atmosphere into box 2 causes a weaker mean THC, which reduces the time of quasi equilibrium # 3 (no sea ice). Fig. 25 shows an example where the fresh water flux is increased.

5.8 Land ice size and purge timescale

As discussed in section 4, the area of the ice sheet has direct impact on the amount of fresh water flux released during the purge stage. There is currently no clear evidence for the size of the area that took place in these collapses. For the LIS we use a 1 million sq. km. area, which is equivalent to much of Hudson Bay and the Foxe Basin. Nevertheless even when taking a third of this size or a few times larger, the cycle does not change significantly, thus our system is not sensitive to this choice. Following MacAyeal we used a typical purge timescale of 250 years, based on evidence from the IRD layers. Experimenting with this parameter we found that for a very large range 25-

1000 years, it affects only the time scale of the purge and has hardly any other effect on the system. The third parameter used in the land ice model is Z_0, the accumulation rate scale height, again we used the parameter chosen by MacAyeal, which corresponds to the accumulation rates from other sources Cuffey and Clow (1997). Increasing this parameter causes a higher accumulation rate which will cause the glacier to be larger by the time the purge begins. This will cause a stronger purge, but does not have a major effect on our mechanism. Varying the upper temperature boundary was discussed in section 4.

5.9 Summary of parameter sensitivity

We presented here a thorough analysis of all parameters used in our model and showed that our model is quite robust. We can divide all parameters into three major categories.

1. The heat/salinity advection/diffusion, THC and meridional coefficients: These parameters mainly determine the timescales of the quasi equilibrium states. They determine the strength of the THC, and the amount of heat transfered by advection or by diffusion. They are important in the sense that they determine the physical quantities of this model, but as we saw they can compensate for one another so a single choice of parameter is not that important. Although these time scales are important when comparing our model to the data, we see here that they have no major effect on the physical mechanism

2. Energy balance parameters: These are parameters which characterize our model. They come into the model to play a role in the energy balance and describe the existing differences between for instance the albedo of ocean and the albedo of sea ice. A specific choice of parameter is not important but the relations between them are.

3. Sea ice parameters: Since the quasi equilibrium states are based on sea ice equilibrium, these parameters determine the rate of transition between the equilibria states. Since the model is very simplified we expect the transitions to be quick (if we would have more boxes we may have had longer transition times or more intermediate states), therefore the choice of these parameters is important only in giving the physical quantities and the transition time scales a reasonable value.

6 Conclusion

Using a simple coupled atmosphere, ocean, and sea ice box model, and MacAyeal's binge-purge ice sheet oscillator we presented here a novel mechanism for Heinrich events; The purge stage causes a fresh water flux into the northern Atlantic, causing a weakening of the THC. In response, after the purge is over, a flush in the THC occurs, due to strong diffusion into the low salinity northern ocean and a positive advection feedback by the increasing THC. This flush causes massive melting

of sea ice and abrupt atmospheric heating due to the the strong sea ice albedo effect. The system settles back to equilibrium over a time scale of thousands of years, creating a 7 kyr cycle, dictated by the time scale of the oscillating ice sheet.

In addition we demonstrate that different ice sheets oscillating independently but affecting the ocean via their fresh water flux, and affected by the same atmosphere, become phase locked and synchronized. This may explain the many evidence of synchronized events presented by Bond and Lotti (1995); Elliot et al. (1998); Fronval et al. (1995); Bischof (1994); McCabe and Clark (1998) and others. We have also shown that there may be higher order phase locking scenarios, suggesting some possible relation to the higher frequency D/O events.

The parameter sensitivity analysis has shown that the timescales of the different stages of our model are parameter dependent to some extent, but for a reasonable parameter choice we find that our model matches well the observed data from GRIP Dansgaard et al. (1993) and the IRD layers Heinrich (1988); Broecker et al. (1992); Bond et al. (1992). Also the flushes and the sea ice melting have evidence in core records Elliot et al. (1998).

The purpose of the present model, being highly idealized, is to present a simple mechanism which may explain the Heinrich events. Nevertheless the building blocks of this model have been independently observed in some other models, such as Winton and Sarachik (1993) (THC flushes), and Thorndike (1992) (massive changes in sea ice cover as a result of changes in the ocean heat budget) . We therefore feel this model may be relevant to the observed Heinrich events in spite of its simplicity.

A Appendix

The following appendices provide the more detailed derivation of some of the relations used in the above text.

A.1 The heat equation for the ice sheet

The ice sheet heat equation, is a diffusion equation (neglecting advection terms)

$$\frac{\partial T(t,z)}{\partial t} = \frac{\kappa}{C p_{ice} \rho_{ice}} \frac{\partial^2 T(t,z)}{\partial z^2} \tag{35}$$

Changing the variable z to the independent variable ζ , when $\zeta = \frac{z}{H(t)}$ we get

$$\frac{\partial T(t,z)}{\partial t} = \frac{\partial T(t,\zeta)}{\partial t} + \frac{\partial T(t,\zeta)}{\partial \zeta(t)} \frac{\partial \zeta(t)}{\partial t} = \frac{\partial T(t,\zeta)}{\partial t} + \frac{\partial T(t,\zeta)}{\partial \zeta(t)} \frac{\partial \zeta(t)}{\partial H(t)} \frac{\partial H(t)}{\partial t} =$$

$$
\begin{aligned}
&= \frac{\partial T(t,\zeta)}{\partial t} - \frac{\partial T(t,\zeta)}{\partial \zeta(t)} \frac{\partial H(t)}{\partial t} \frac{\zeta(t)}{H(t)} \\
\frac{\partial T(t,z)}{\partial z} &= \frac{\partial T(t,\zeta)}{\partial \zeta(t)} \frac{\partial \zeta(t)}{\partial z} = \frac{\partial T(t,\zeta)}{\partial \zeta(t)} \frac{1}{H(t)} \\
\frac{\partial T^2(t,z)}{\partial z^2} &= \frac{\partial T^2(t,\zeta)}{\partial \zeta(t)^2} \frac{1}{H(t)^2}
\end{aligned}
$$

Thus the heat equation will have the form

$$
\frac{\partial T(t,\zeta)}{\partial t} = \frac{\kappa}{Cp_{ice}\rho_{ice}H(t)^2} \frac{\partial^2 T(t,\zeta)}{\partial \zeta(t)^2} + \frac{\partial T(t,\zeta)}{\partial \zeta(t)} \frac{\zeta(t)}{H(t)} \frac{\partial H(t)}{\partial t} \tag{36}
$$

For the binge stage, inserting (1) in (36) will give

$$
\frac{\partial T(t,\zeta)}{\partial t} = \frac{\kappa}{Cp_{ice}\rho_{ice}H(t)^2} \frac{\partial^2 T(t,\zeta)}{\partial \zeta(t)^2} + \frac{\partial T(t,\zeta)}{\partial \zeta(t)} \frac{\zeta(t)(Acc - Abl)}{H(t)}
$$

and in the purge stage, inserting (7) will give

$$
\frac{\partial T(t,\zeta)}{\partial t} = \frac{\kappa}{Cp_{ice}\rho_{ice}H(t)^2} \frac{\partial^2 T(t,\zeta)}{\partial \zeta(t)^2} - \frac{\partial T(t,\zeta)}{\partial \zeta(t)} \frac{\zeta(t)}{\tau}
$$

A.2 The ocean momentum equations

Beginning with the Naiver-Stokes equation for a rotating fluid Pedlosky (1987, Chapter 1.6)

$$
\left[\frac{d\mathbf{u}}{dt} + 2\Omega \times \mathbf{u} \right] \rho = -\nabla p + \rho \nabla \Phi + F
$$

where $\mathbf{u}$ is the fluid vector velocity, ρ is it's density, Ω is the rotation frequency so $2\Omega \times \mathbf{u}$ is the Coriolis acceleration. ∇p is the pressure gradient force, and $\rho \nabla \Phi$ is the body force. We assume that a fluid element only feels gravity. The body force is therefore ρg, where g is the gravitational acceleration. F is the frictional force in the fluid, since ocean water are nearly Newtonian we can take F as

$$
F = \eta \nabla^2 \mathbf{u} + \frac{\eta}{3} \nabla (\nabla \cdot \mathbf{u})
$$

where η is the molecular viscosity.

Under the Boussinesq approximation, we assume ρ_0 is a constant desity and the second term in F vanishes ($\nabla \cdot \mathbf{u} = 0$ incompressibility). Parameterizing friction by a Rayleigh form we take

$\nabla^2 \to -r$, where r is some constant. Therefore the equation may now be written as:

$$\left[\frac{\partial \mathbf{u}}{\partial t} + (\mathbf{u}\cdot\nabla)\mathbf{u} + 2\Omega \times \mathbf{u}\right]\rho_0 = -\nabla p + \rho g - r\mathbf{u}$$

In component form, taking $\mathbf{u} = (u, v, w)$ we find

$$\left[\frac{\partial u}{\partial t} + u\frac{\partial u}{\partial x} + v\frac{\partial u}{\partial y} + w\frac{\partial u}{\partial z} - fv\right]\rho_0 = -\frac{\partial p}{\partial x} - ru \tag{37}$$

$$\left[\frac{\partial v}{\partial t} + u\frac{\partial v}{\partial x} + v\frac{\partial v}{\partial y} + w\frac{\partial v}{\partial z} + fu\right]\rho_0 = -\frac{\partial p}{\partial y} - rv \tag{38}$$

$$\left[\frac{\partial w}{\partial t} + u\frac{\partial w}{\partial x} + v\frac{\partial w}{\partial y} + w\frac{\partial w}{\partial z}\right]\rho_0 = -\frac{\partial p}{\partial z} + \rho g - rw \tag{39}$$

where f is the Coriolis parameter, and the rotation axis coincides with the z axis as in the shallow water model Pedlosky (1987, Chapter 3.2). In our model we do not have an East-West velocity, therefore the first equation and all terms containing u are taken as zero. Also we assume quasi-stationary motion such that the velocity changes in time are very small, so we neglect the time dependent terms.

From the condition of incompressibility

$$\frac{\partial u}{\partial x} + \frac{\partial v}{\partial y} + \frac{\partial w}{\partial z} = 0$$

we see that the scale of the first two terms is $O(\frac{U}{L})$ where U is the characteristic scale of the horizontal velocity and L is the characteristic horizontal scale of motion. If W is the scale of the vertical velocity, and D is the vertical scale of motion, it follows that the $\frac{W}{D}$ can be no larger than $O(\frac{U}{L})$, meaning

$$W < O(\frac{DU}{L}).$$

Applying the characteristic scales used in ocean models

$$\begin{aligned} L &= O(10^6 m) \\ D &= O(10^2 m) \\ U &< O(1\frac{m}{s}) \end{aligned}$$

we see that the vertical velocity's scale is $O(10^{-4})$, so compared to the horizontal velocity it is negligible in this model. Also the nonlinear terms on the left side of (38) have a scale of no more than $O(10^{-3})$. From (47) we see that in our model $r \cong 0.008\frac{Kg}{m^3 sec}$, so the term rv is at least 8 times

the nonlinear terms on the left side of (38), so for the horizontal momentum balance we are left with

$$\frac{\partial p}{\partial y} = -rv$$

In a similar fashion following Pedlosky (1987, Chapter 3.2), neglecting the nonlinear terms and the smaller w dependent terms, we get the hydrostatic approximation from (39)

$$\frac{\partial p}{\partial z} = -\rho g$$

A.3 The THC as function of the ocean box densities

From the Navier-Stokes equation we found (13) and (14). Integrating (13) over the upper boxes gives

$$WD_{upper}(P_2 - P_1) = rU(L_1 + L_2) \tag{40}$$

where U is the transport defined as positive in the northward and upward directions meaning

$$U = WD_{upper}v_{upper} = -WL_{north}w_{north} = -WD_{lower}v_{lower} = WL_{south}w_{south} \tag{41}$$

therefore integrating over the lower boxes, comparing to (40) and using $\delta = \frac{D_{upper}}{D_{lower}}$ gives

$$\delta(P_2 - P_1) = P_4 - P_3 \tag{42}$$

Integrating the hydrostatic approximation (14), over each box while assuming a surface pressure over the surface boxes of amplitude η_i and density ρ_0 gives

$$\begin{aligned} P_1 &= \frac{1}{2}\rho_1 g D_u + \eta_1 \rho_0 \\ P_2 &= \frac{1}{2}\rho_2 g D_u + \eta_2 \rho_0 \\ P_3 &= \frac{1}{2}\rho_3 g D_l + \rho_2 g D_u + \eta_2 \rho_0 \\ P_4 &= \frac{1}{2}\rho_4 g D_l + \rho_1 g D_u + \eta_1 \rho_0 \end{aligned} \tag{43}$$

where the box pressure was average in the middle of each box, and we have used the short notation D_u, D_l for D_{upper} and D_{lower} respectively. Inserting (43) into (42) gives

$$\eta_1 - \eta_2 = \frac{gD_d}{\rho_0(1+\delta)}\left[\delta(1+\frac{\delta}{2})(\rho_2 - \rho_1) + \frac{1}{2}(\rho_3 - \rho_4)\right]. \tag{44}$$

From (40) and (43) we find

$$U = \frac{-WD_u}{r(L_1+L_2)}\left[\frac{1}{2}\rho_2 D_u(\rho_2-\rho_1)+\rho_0(\eta_2-\eta_1)\right]. \tag{45}$$

Inserting (44) into (45) gives

$$U = \frac{WD_u g}{2r(L_1+L_2)(1+\delta)}\left[(\rho_2-\rho_1)D_u+(\rho_3-\rho_4)D_l\right] \tag{46}$$

which is the expression we use in (15), where

$$C_u = \frac{WD_u}{2r(L_1+L_2)(1+\delta)} \tag{47}$$

A.4 Saturation humidity as function of atmospheric temperature

The fresh water flux is derived from the Clausius-Clapeyron relation

$$\frac{de_s}{dT} = \frac{0.622Le_s}{R_d T^2} \tag{48}$$

where e_s is the saturation vapor pressure, R_d the gas constant for dry air and L is the latent heat of evaporation. Thus the vapor pressure is given by

$$e_s = C_q e^{\frac{-L}{R_d T}}. \tag{49}$$

The saturation specific humidity is defined as

$$q_s = \frac{0.622e_s}{p}, \tag{50}$$

where p is the pressure of moist air given as

$$p = \rho R_d T(1+0.61q) \tag{51}$$

Under the approximation $p \cong \rho R_d T = p_0$,the surface atmospheric pressure, the saturation humidity becomes

$$q_s = 0.622 \cdot C_q e^{\frac{-L}{R_d T}}. \tag{52}$$

In terms of potential temperature 52 gives

$$q_s = 0.622 \cdot C_q e^{\frac{-2\frac{R_d}{C_{p_{air}}}\cdot L}{R_d \theta}} = C_{mer} \cdot e^{\frac{-L}{R_d T}}$$

B Table of variables in the model

Variabls	Meaning	Units	Model (O,A,L)
$T_i(t)$	Ocean temperature in box i	^oC	O
$S_i(t)$	Salinity in box i	$grKg^{-1}$(none)	O
$\rho_i(t)$	Water density in box i	Kgm^{-3}	O
$\theta_i(t)$	Atmosphere potential temperature in box i	^oC	A,O,L
$H(t)$	Height of glacier at time t	m	L
$T(t,\zeta)$	Temperature of glacier at t and $0<\zeta<1$	^oC	L
$Acc(t)$	Accumulation rate on top of the glacier	ms^{-1}	L
$Abl(t)$	Ablation rate on top of the glacier	ms^{-1}	L
$U(t)$	Transport	m^3s^{-1}	O
$(Q_T)_i^{atm-ocean}(t)$	Heat flux between Atm. and Ocean	m^oCs^{-1}	O,A
$(Q_T)_i^{seaice-ocean}(t)$	Heat flux between sea ice and Ocean	m^oCs^{-1}	O
$(Q_S)_i^{atm-ocean}(t)$	Fresh water flux from Atm. to land/Ocean	ms^{-1}	A,O,L
$(Q_S)_i^{seaice-ocean}(t)$	Fresh water flux from sea ice to Ocean	ms^{-1}	O
$(Q_S)_i^{landice-ocean}(t)$	Fresh water flux from land ice to Ocean	ms^{-1}	O,L
$V_i^{seaice}(t)$	Volume of sea ice	$meter^3$	O
$P^{on-ice}(t)$	Accumulation of sea ice directly from precip.	ms^{-1}	O
$frac^{seaice}(t)$	Fraction of seaice area out of ocean box area	none	O,A
$thickness(t)$	Thickness of the seaice in the box	$meter$	O
$\alpha_i^{tot}(t)$	Average albedo of box i	none	A
$SW_i(t)$	Shortwave radiation	$Watt\,m^{-2}$	A
$LW_i(t)$	Longwave radiation	$Watt\,m^{-2}$	A
$SW_i^{seaice}(t)$	Shortwave radiation dirctly meltig sea ice	$Watt\,m^{-2}$	A,O
$q_s(t)$	Saturtation specific humidity	none	A

References

Alley, R. (1998). Icing the North Atlantic. *Nature*, 392:335–336.

Alley, R., Anandakrishnan, S., and Jung, P. (2001). Stochastic resonance in the north atlantic. *Paleoceanography*, 16(2):190–198.

Alley, R. and MacAyeal, D. (1994). Ice-rafted debris associated with binge/purge oscillations of the laurentide ice sheet. *Paleoceanography*, 9(4):503–511.

Bischof, J. (1994). The decay of the barents ice sheet as documented in the nordic seas ice-rafted debris. *Marine Geology*, 117:35–55.

Bond, G., Broecker, W., Johnsen, S. J., McManus, J., Labeyrie, L., Jouzel, J., and Bonani, G. (1993). Correlations between climate records from North Atlantic sediments and the Greenland ice. *Nature*, 365:143–147.

Bond, G., Heinrich, H., Broecker, W., Laberie, L., McManus, J., Andrews, J., Huon, S., Jantschik, R., Clasen, S., Simet, C., Tedesco, K., Klas, M., Bonani, G., and Ivy, S. (1992). Evidence for massive discharges of icebergs into the North Atlantic Ocean during the last glacial period. *Nature*, 360(6401):245–249.

Bond, G. and Lotti, R. (1995). Iceberg discharges into the North Atlantic on millennial time scales during the last glaciation. *Science*, 267:1005–1009.

Braithwate, R. (1981). On glacier energy balance, ablation, and air temperature, journal of glaciology. *J. of Glaciology*, 27(97).

Broecker, W., Bond, G., Klas, M., Bonani, B., and Wolfi, W. (1990). A salt oscillator in the glacial Atlantic?- the concept. *Paleoceanography*, 5:469–478.

Broecker, W., Bond, G., Klas, M., Clark, E., and McManus, J. (1992). Origin of the northern Atlantic's Heinrich events. *Clim. Dyn.*, 6:265–273.

Broecker, W. S., Bond, G., Klas, M., Clark, E., and McManus, J. (1992). Origin of the northern Atlantic's Heinrich events. 6:265–273.

Broecker, W. S. and Hemming, S. (2001). Climate swings come into focus. *Science*, 294:2308–2309.

Bryan, K., Manabe, S., and Pacanowski, R. (1974). A global ocean-atmosphere climate model. part 2. the oceanic circulation. *J. Phys. Oceanogr.*, 5:30–46.

Cuffey, K. and Clow, G. (1997). Temperature, accumulation, and ice sheet elevation in central Greenland through the last deglacial transition. *J. Geophys. Res.*, 102:26,383–26,396.

Dansgaard, W., Johnsen, S. J., Clausen, H. B., Dahl-Jensen, D., Gundestrup, N., Hammer, C. U., and Oescger, H. (1984). North Atlantic climate oscillations revealed by deep Greenland ice cores. In Hansen, J. E. and Takahashi, T., editors, *Climate Processes and Climate Sensitivity*, volume 5 of *Geophysical Monographs*, pages 288–298, Washington D.C. American Geophysical Union.

Dansgaard, W., Johnsen, S. J., Clausen, H. B., Dahl-Jensen, D., Gundestrup, N., Hammer, C. U., Steffensen, J. P., Sveinbjornsdottir, A. E., Jouzel, J., and Bond, G. (1993). Evidence for general instability of past climate from a 250-kyr ice-core record. *Nature*, 364:218–220.

Dowdeswell, J., Elverhoi, A.and Andrews, J., and Hebbein, D. (1999). Asynchronous deposition of ice-rafted layers in the nordic seas and north atlantic ocean. *Nature*, 400:348–351.

Elliot, M., Labeyrie, L., Bond, G., Cortijo, E., Turon, J., Tisnerat, N., and Duplessy, J. (1998). Millennial-scale iceberg discharges in the irminger basin during the last glacial period: Relationship with the heinrich events and environmental settings. *Paleoceanography*, 13:433–446.

Fronval, T., Jansen, E., Bloemendal, J., and Johnsen, S. (1995). Oceanic evidence for coherent fluctuations in fennoscandian and laurentide ice sheets on millennium timescales. *Nature*, 374:443–446.

Ganopolski, A. and Rahmstorf, S. (2001). Rapid changes of glacial climate simulated in a coupled climate model. *Nature*, 409:153–158.

Gildor, H. and Tziperman, E. (2001). A sea-ice climate-switch mechanism for the 100 kyr glacial cycles. *J. Geophys. Res.*, 106(C5):9117–9133.

Gill, A. E. (1982). *Atmosphere–ocean dynamics*. Academic Press, London.

Heinrich, H. (1988). Origin and consequences of cyclic ice rafting in the Northeast Atlantic Ocean during the past 130,000 years. *Quat. Res.*, 29:142–152.

Jones, G. and Keigwin, L. (1988). Evidence from fram strait (78 n) for early deglaciation. *Nature*, 336:56–59.

Källén, E., Crafoord, C., and Ghil, M. (1979). Free oscillations in a climate model with ice-sheet dynamics. *J. Atmos. Sci.*, 36:2292–2303.

Legrand, P. and Wunsch, C. (1995). Constraints from paleotracer data on the North-Atlantic circulation during the Last Glacial Maximum. *Paleoceanography*, 10(6):1011–1045.

MacAyeal, D. (1989). Large-scale ice flow over a viscous basal sediment: Theory and application to ice stream b, antarctica. *J. Geophys. Res.*, 94:4071–4087.

MacAyeal, D. (1993a). Binge/purge oscillations of the laurentide ice-sheet as a cause of the North-Atlantics Heinrich events. *Paleoceanography*, 8(6):775–784.

MacAyeal, D. (1993b). A low-order model of the Heinrich Event cycle. *Paleoceanography*, 8(6):767–773.

Marotzke, J., Welander, P., and Willebrand, J. (1988). Instability and multiple steady states in a meridional-plane model of the thermohaline circulation. *Tellus*, 40A:162–172.

Maykut, G. and Perovich, D. (1987). The role of shortwave radiation in summer decay of a sea ice cover. *J. Geophys. Res.*, 92:7032–7044.

McCabe, A. and Clark, P. (1998). Ice-sheet variability around the north atlantic ocean during the last deglaciation. *Nature*, 392:373–377.

Pedlosky, J. (1987). *Geophysical Fluid Dynamics*. Springer-Verlag, Berlin-Heidelberg-New York., 2 edition.

Peixoto, J. and Oort, A. (1991). *Physics of Climate*. American Institute of Physics, New York.

Rivin, I. and Tziperman, E. (1997). Linear versus self-sustained interdecadal thermohaline variability in a coupled box model. *J. Phys. Oceanogr.*, 27(7):1216–1232.

Stocker, T., Wright, D., and Broecker, W. (1992). The influence of high-latitude surface forcing on the global thermohaline circulation. *Paleoceanography*, 7(5):529–541.

Stommel, H. (1961). Thermohaline convection with two stable regimes of flow. *Tellus*, 13:224–230.

Thorndike, A. (1992). A toy model linking atmospheric thermal radiation and sea ice growth. *J. Geophys. Res.*, 97:9401–9410.

Timmermann, A., Gildor, H., Schulz, M., and Tziperman, E. (2002). Coherent resonant millennial-scale climate oscillations triggered by massive meltwater pulses. *J. Climate*. submitted.

Trenberth, K., editor (1992). *Climate System Modeling*. Cambridge University Press.

Tziperman, E. and Gildor, H. (2002). The stabilization of the thermohaline circulation by the temperature-precipitation feedback. *J. Phys. Oceanogr.*, 32:2707–2714.

Walsh, J. (1982). The role of sea ice in climate variability: theories and evidence. *Atmosphere-ocean*, 21:229–242.

Winton, M. and Sarachik, E. S. (1993). Thermohaline oscillation induced by strong steady salinity forcing of ocean General Circulation Models. *J. Phys. Oceanogr.*, 23:1389–1410.